Cell Reports

Endophilin-A Deficiency Induces the Foxo3a-Fbxo32 Network in the Brain and Causes Dysregulation of Autophagy and the Ubiquitin-Proteasome System

Graphical Abstract

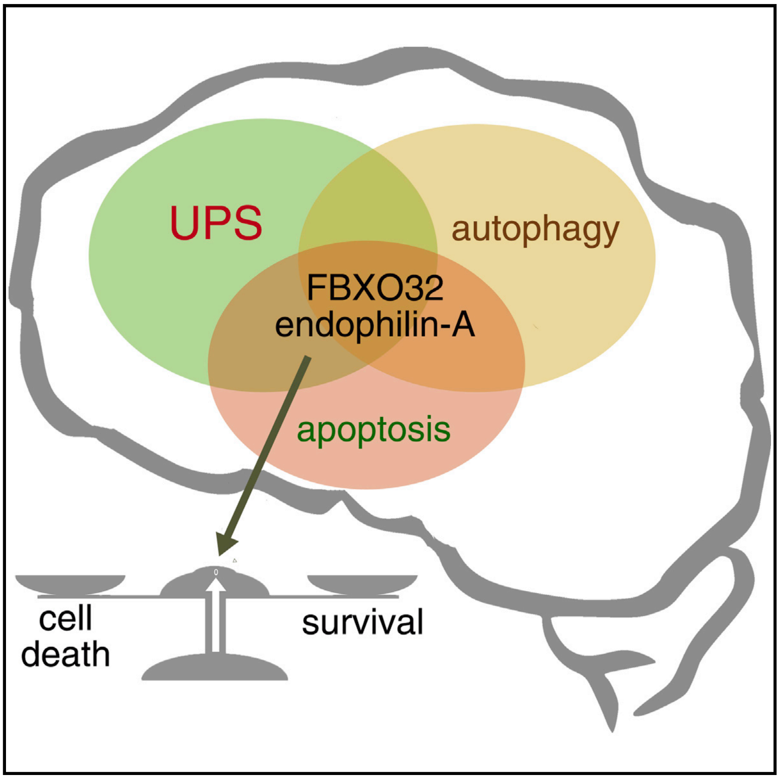

Authors

John D. Murdoch, Christine M. Rostosky, Sindhuja Gowrisankaran, ..., Stefan Bonn, Nuno Raimundo, Ira Milosevic

Correspondence

nuno.raimundo@med.uni-goettingen.de (N.R.),
imilose@gwdg.de (I.M.)

In Brief

Regulation of protein homeostasis and autophagy has become a promising line of research in the neurodegeneration field. Murdoch et al. now find that endophilin-A, a key factor in clathrin-mediated endocytosis, regulates protein homeostasis through the Foxo3a-Fbxo32 network.

Highlights

- Endophilin-A is needed for autophagosome formation in mammalian neurons and brain
- Absence of endophilin-A upregulates the E3-ubiquitin ligase FBXO32
- FBXO32-endophilin-A interaction maintains neuronal health and protein homeostasis
- Endophilin-A KO mice show age-dependent ataxia, motor impairments, and neurodegeneration

Accession Numbers

GSE85702

Murdoch et al., 2016, Cell Reports *17*, 1071–1086
October 18, 2016 © 2016 The Author(s).
http://dx.doi.org/10.1016/j.celrep.2016.09.058

Cell Reports
Article

OPEN
ACCESS
CellPress

Endophilin-A Deficiency Induces the Foxo3a-Fbxo32 Network in the Brain and Causes Dysregulation of Autophagy and the Ubiquitin-Proteasome System

John D. Murdoch,[1,2,8] Christine M. Rostosky,[1,8] Sindhuja Gowrisankaran,[1] Amandeep S. Arora,[1]
Sandra-Fausia Soukup,[3,4] Ramon Vidal,[5] Vincenzo Capece,[5] Siona Freytag,[1] Andre Fischer,[6,7] Patrik Verstreken,[3,4]
Stefan Bonn,[5] Nuno Raimundo,[2,*] and Ira Milosevic[1,9,*]
[1]European Neuroscience Institute (ENI), 37077 Göttingen, Germany
[2]Institute of Cellular Biochemistry, University Medical Center Göttingen (UMG), 37073 Göttingen, Germany
[3]VIB Center for Brain & Disease Research, 3000 Leuven, Belgium
[4]KU Leuven Department of Human Genetics, Leuven Institute for Neurodegenerative Disease (LIND), 3000 Leuven, Belgium
[5]Computational Systems Biology, German Center for Neurodegenerative Diseases (DZNE), 37077 Göttingen, Germany
[6]Epigenetics and Systems Medicine in Neurodegenerative Diseases, German Center for Neurodegenerative Diseases (DZNE), 37077 Göttingen, Germany
[7]Department of Psychiatry and Psychotherapy, University Medical Center Göttingen, 37077 Göttingen, Germany
[8]Co-first author
[9]Lead Contact
*Correspondence: nuno.raimundo@med.uni-goettingen.de (N.R.), imilose@gwdg.de (I.M.)

http://dx.doi.org/10.1016/j.celrep.2016.09.058

SUMMARY

Endophilin-A, a well-characterized endocytic adaptor essential for synaptic vesicle recycling, has recently been linked to neurodegeneration. We report here that endophilin-A deficiency results in impaired movement, age-dependent ataxia, and neurodegeneration in mice. Transcriptional analysis of endophilin-A mutant mice, complemented by proteomics, highlighted ataxia- and protein-homeostasis-related genes and revealed upregulation of the E3-ubiquitin ligase FBXO32/atrogin-1 and its transcription factor FOXO3A. FBXO32 overexpression triggers apoptosis in cultured cells and neurons but, remarkably, coexpression of endophilin-A rescues it. FBXO32 interacts with all three endophilin-A proteins. Similarly to endophilin-A, FBXO32 tubulates membranes and localizes on clathrin-coated structures. Additionally, FBXO32 and endophilin-A are necessary for autophagosome formation, and both colocalize transiently with autophagosomes. Our results point to a role for endophilin-A proteins in autophagy and protein degradation, processes that are impaired in their absence, potentially contributing to neurodegeneration and ataxia.

INTRODUCTION

The nervous system relies on conserved endocytic and synaptic vesicle (SV) recycling mechanisms to sustain high activity. Defective endocytosis and SV recycling have long been implicated in neurodegeneration and neurodegenerative diseases, yet the molecular mechanisms remain unclear (Esposito et al., 2012; Heutink and Verhage, 2012; Saheki and De Camilli, 2012; Schreij et al., 2016).

Endophilin-A (henceforth endophilin) endocytic adaptors are key players in membrane dynamics at the neuronal synapse (Ringstad et al., 1999; Verstreken et al., 2002; Milosevic et al., 2011; Saheki and De Camilli, 2012). Endophilin-1 and 3 are brain-specific, whereas endophilin-2 is ubiquitous (Ringstad et al., 1997, 1999). All three contain a highly conserved BAR domain and have a central role in both clathrin-mediated endocytosis (Farsad et al., 2001; Ringstad et al., 1997, 1999, 2001; Verstreken et al., 2002; Milosevic et al., 2011) and clathrin-independent endocytosis (Boucrot et al., 2015). In clathrin-mediated endocytosis, endophilin recruits synaptojanin-1 to the necks of coated vesicles prior to scission by dynamin (Milosevic et al., 2011). Furthermore, availability of endophilin is rate limiting for vesicle uncoating and SV recycling, and neurons without endophilin show reduced neurotransmission (Milosevic et al., 2011).

Total absence of endophilin is perinatally lethal, whereas mice lacking endophilin-1 and 2 (1,2 double knockout [DKO]) show ataxia, neurodegeneration, and early lethality (Milosevic et al., 2011). Why this happens is an intriguing question. It cannot be easily explained by defective neurotransmission, because even mice with paralysis and abolished neurotransmission do not develop neurodegeneration (Heutink and Verhage, 2012). Thus, it is unlikely that neurodegeneration in endophilin 1,2 DKO mice is solely the result of defective SV recycling.

Mice without endophilin also show increased protein ubiquitination (Cao et al., 2014), and neurodegeneration is frequently associated with impaired proteolytic systems, most notably the ubiquitin-proteasome system (UPS) and autophagy (Nakamura and Lipton, 2009; Nixon, 2013; Menzies et al., 2015). Endophilin has been linked to the UPS through direct interaction with the

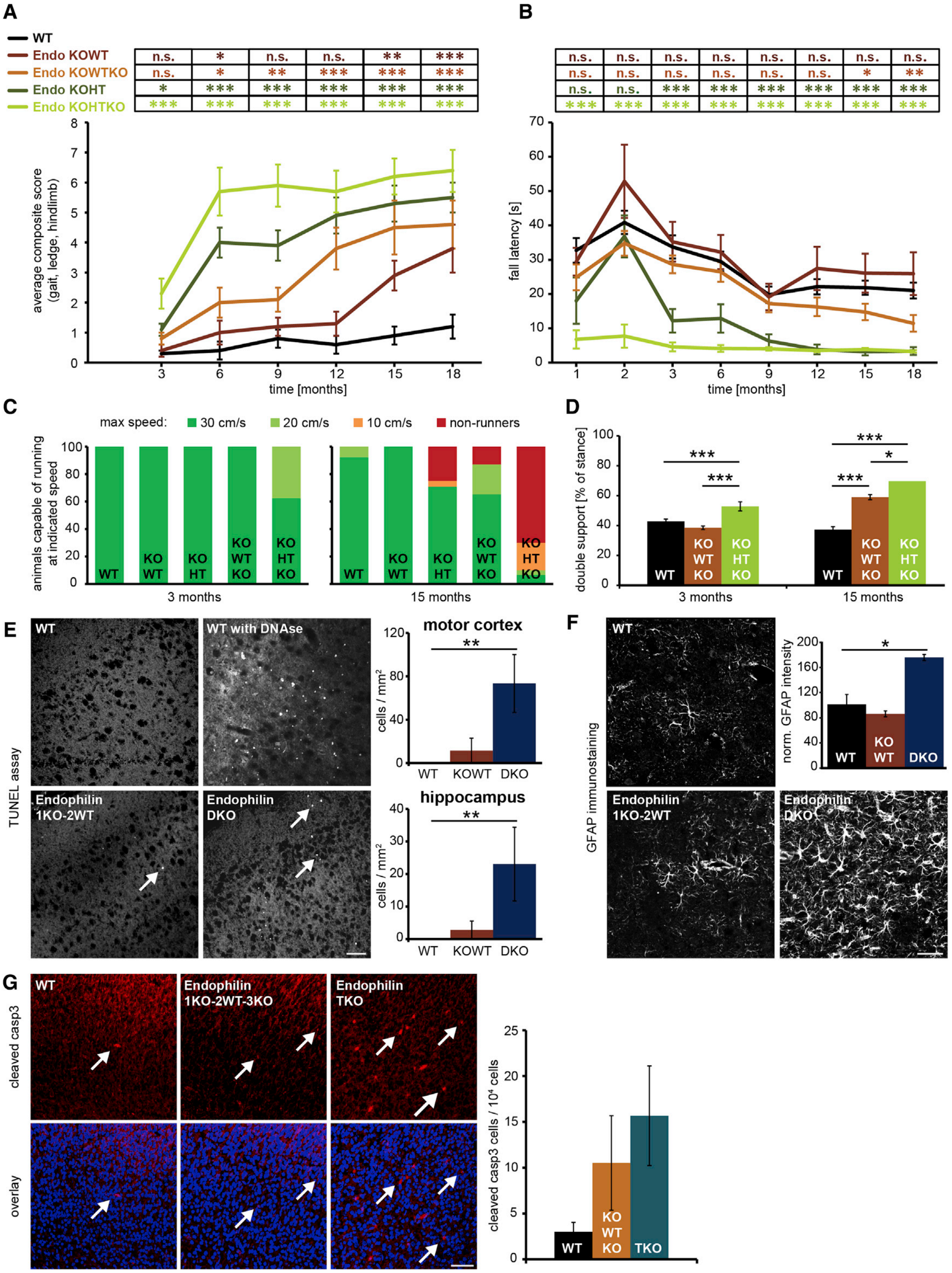

Figure 1. Endophilin Deficiency Causes Age-Dependent Motor Impairments in Mice

(A) Endophilin mutant mice exhibit progressive ataxia in which onset depends on severity of endophilin deficiency. Mice were assessed on a 0–3 scale for ledge test, clasping, gait, and kyphosis from 3 to 18 months. Eight to twelve mice/genotype are shown. Average composite score for each indicated genotype at defined age was calculated; mean ± SEM (two-way ANOVA; $***p < 0.001$; $**p < 0.01$; $*p < 0.05$; ns > 0.05).

(B) Rotarod performance plotted as latency to fall. Motor coordination was assessed at 1–18 months. After a training session (not shown), fall latency from the accelerating rod was measured for the same genotypes as in (A). Mean ± SEM; min. eight mice/genotype; Student's t test; $***p < 0.001$.

(legend continued on next page)

Parkinson's disease (PD)-related E3-ubiquitin ligase parkin (Trempe et al., 2009) and as a key component of the CBL-CIN85-endophilin complex known to downregulate receptors (Soubeyran et al., 2002; Petrelli et al., 2002).

Additional links between endophilin and neurodegeneration have recently emerged. The most commonly disrupted gene in familial PD (Cookson, 2010), *LRRK2*, encodes a protein that phosphorylates endophilin (Matta et al., 2012). LRRK2 appears in Lewy bodies and plays a role in apoptosis and autophagy (Iaccarino et al., 2007; Tong et al., 2012). In addition, a number of case studies described synaptojanin-1 and auxilin mutations in early-onset parkinsonism (Edvardson et al., 2012; Quadri et al., 2013; Krebs et al., 2013). Auxilin is recruited to the clathrin-coated vesicles directly after the action of synaptojanin-1, which is brought to the neck of the clathrin-coated pit by endophilin (Milosevic et al., 2011). Interestingly, endophilin is upregulated in the brains of PD patients (Shi et al., 2009). In addition, endophilin-1 and 3 have been shown to interact with ataxin-2, mutations in which lead to spinocerebellar ataxia type 2 (Ralser et al., 2005; Nonis et al., 2008).

Despite direct parkin-endophilin interaction and a striking upregulation of parkin in mice lacking all three endophilin genes (endophilin triple knockout [TKO]; Cao et al., 2014), elevated parkin could not explain the endophilin-deficient phenotype. We subjected endophilin mutants to RNA sequencing and found upregulation of another E3-ubiquitin ligase, F-box-only protein 32 (*Fbxo32*, also called atrogin-1/MAFbx). FBXO32 has previously been studied in muscles, where its induction occurs prior to the onset of rapid atrophy (Sandri et al., 2004). While studying how the FBXO32-endophilin-A interaction balances protein degradation and neuronal health in the brain, we discovered a direct role of endophilin-A in autophagosome formation.

RESULTS

Endophilin-A Deficiency Results in Age-Dependent Movement Impairments in Mice

Mice lacking all three endophilin genes die perinatally, whereas endophilin 1,2 DKO animals show ataxia, neurodegenerative changes, and lethality around 3 weeks (Movie S1; Milosevic et al., 2011). Whereas single knockout (KO) and heterozygous (1HT-2HT; 1HT-2HT-3HT) mice appear phenotypically normal, endophilin 1KO-2HT, 1KO-2WT-3KO, and particularly 1KO-2HT-3KO mice exhibit shorter lifespans (~19, ~21, and ~18 months, respectively; 1HT-2HT mice lived over 27 months; Figure S1A). Observing 1KO-2HT and 1KO-2HT-3KO mice revealed progressive impairments in motor coordination and increasingly obvious ataxia as these animals age.

To systematically measure the progression of ataxia, we used a composite phenotype scoring system that incorporates hindlimb clasping, ledge walking, kyphosis, and gait (Guyenet et al., 2010). When applied to four endophilin lines (1KO-2WT, 1KO-2HT, 1KO-2WT-3KO, and 1KO-2HT-3KO) and wild-type (WT) controls, it revealed phenotypic differences between endophilin mutants and within the same animals over the course of aging (Figure 1A); i.e., the onset and progression of ataxia correlate with age and severity of endophilin deficiency.

Next, we systematically evaluated locomotion by accelerating rotarod (ARR) performance test and gait analysis. Whereas the performance of 1KO-2WT mice on the ARR was comparable to WT, fall latency in 1KO-2HT-3KO mice was already significantly lower at a very young age (Figure 1B). Intermediate phenotypes were observed in 1KO-2HT and 1KO-2WT-3KO mice, where fall latency compared to WT was decreased significantly at 3 and 15 months, respectively.

Gait analysis revealed that ability to run on a motorized treadmill and walking pattern also depended on the number of missing alleles and age (Figures 1C, 1D, and S1B; see Movie S2). 1KO-2HT-3KO gait was impaired at 3 months, whereas the littermate 1KO-2WT-3KO mice showed impaired gait at 15 months (Figure 1D). Overall, onset and progression of movement impairments correspond to age and the extent of endophilin deficiency.

Neurodegenerative Changes in the Brain of Endophilin-A Mutants

To evaluate whether neurodegenerative changes could cause these motor impairments, we inspected neuronal cell death and gliosis in our model. Whereas overall neuronal cell morphology was unaltered in these mice (Figure S1D), TUNEL assay revealed slightly increased cell death in endophilin 1KO-2WT and more prominently in 1,2 DKO motor cortex and hippocampus at postnatal day (p)18 (Figure 1E). Increased cell death was also found in 18-month 1KO-2HT-3KO motor cortex and hippocampus (Figure S1C). Glial fibrillary acidic protein immunostaining revealed prominent upregulation of gliosis in 1,2 DKO motor cortex (Figure 1F). Because endophilin TKO mice die a few hours after birth, we probed for early markers of apoptosis in endophilin TKO brains and found an increase in caspase 3 activity (Figure 1G). In summary, newborn endophilin TKOs, juvenile 1,2 DKO, and aged 1KO-2HT-3KO mice display signs of mild to moderate neurodegeneration.

(C) Highest speed that endophilin mutants were able to run on DigiGait at 3 (left) and 15 (right) months. Colors represent percentage of mice able to run at indicated speed.

(D) Percentage of time both hindlimbs touch the ground simultaneously while running at 20 cm/s, quantitated for endophilin 1KO-2WT-3KO and 1KO-2HT-3WT mice in comparison to WT. Mean ± SEM, Student's t test, $^{*}p<0.05$, $^{***}p<0.001$.

(E) TUNEL assay on brain sections of mice with indicated genotypes. No apoptotic signal was observed in WTs; cell death was spotted very rarely in endophilin 1KO-2WT brains and more frequently in endophilin 1,2 DKO sections (indicated by arrows). The scale bar represents 50 μm. (Right) Quantification in motor cortex (up) and hippocampus (down) is shown. Mean ± SEM; four mice/genotype.

(F) GFAP immunofluorescence in endophilin 1,2 DKO brain sections showed more gliosis compared to controls. The scale bar represents 20 μm. (Right) Quantification is shown. Mean ± SEM; four mice/genotype.

(G) Immunostaining for cleaved caspase 3 on brain slides of the indicated genotypes. Arrows indicate cells with positive caspase 3 signal. The scale bar represents 50 μm. (Right) Quantification is shown. Mean ± SEM; five mice/genotype.

See also Figure S1 and Movies S1 and S2.

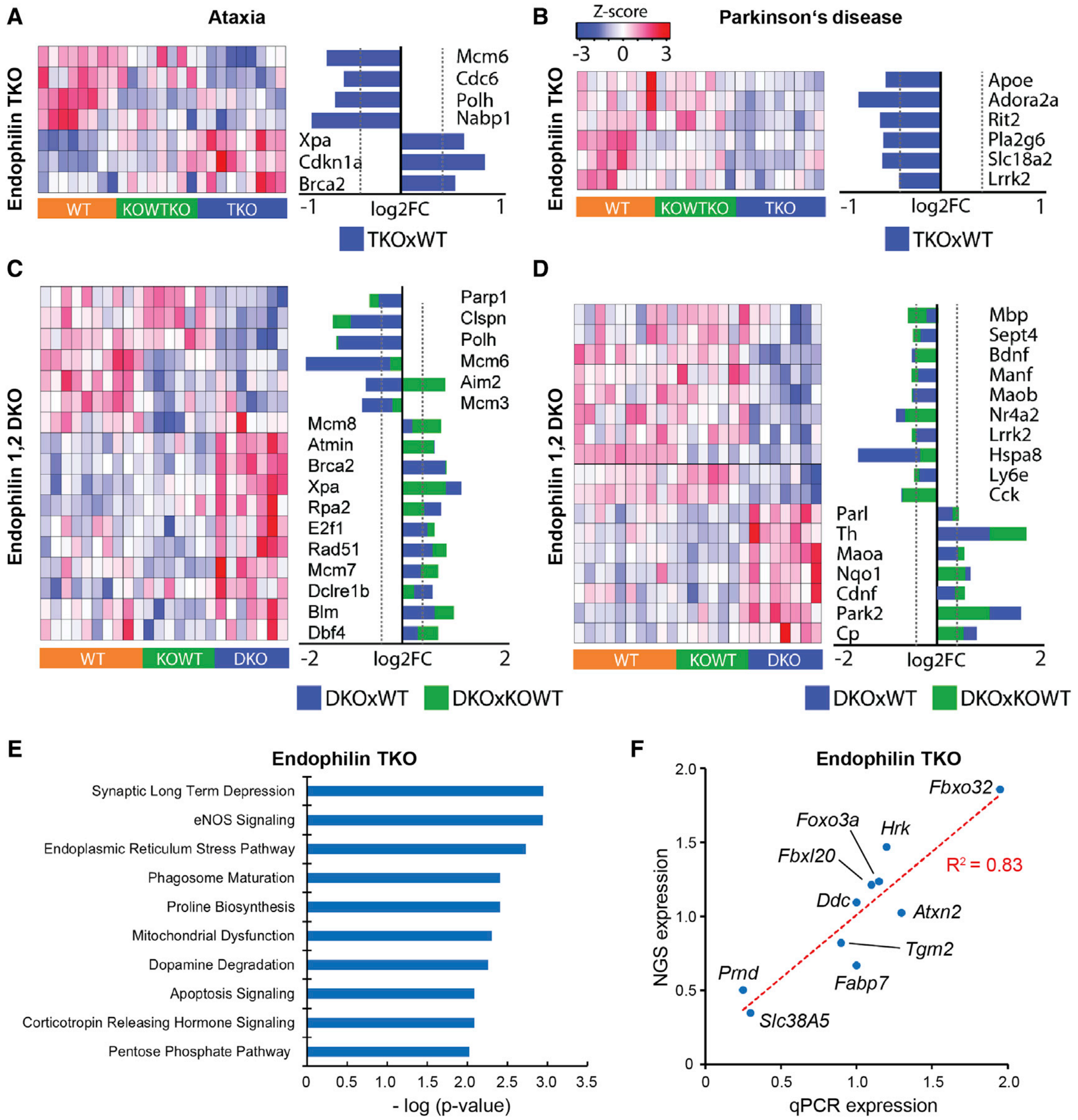

Figure 2. Transcriptional Analysis of Endophilin TKO and 1,2 DKO Hippocampi

(A–D) Heatmap showing the expression of ataxia- (A: TKO; C: 1,2 DKO) and Parkinson's-disease-related genes (B: TKO; D: 1,2 DKO).

(E) Pathway analysis of the transcriptional signatures of TKO hippocampi using the IPA software. The ten most significantly enriched pathways based on Fisher exact test p values (x axis) are presented.

(F) The RNA sequencing results verified by qRT-PCR for named genes in TKO samples.

See also Figure S2 and Tables S1, S2, S3, S4, S5, S6, S7, and S8.

Endophilin-A Deficiency Changes the Expression of Ataxia-, PD -, and Protein-Homeostasis-Related Genes

We were interested in the molecular mechanisms underlying neurodegeneration in our endophilin-deficient models, so we employed RNA sequencing (experimental strategy in Figure S2A). We first sequenced hippocampal RNA from TKO mice that show altered SV recycling and controls (n = 8–9 mice/condition). The data are of high technical quality (~27M aligned reads) and samples clustered well according to genotype (Table S1; Figures S2B and S2C). 182 differentially expressed genes (DEGs) between endophilin TKO and littermate controls and 964 DEGs between TKO and WT were detected (adjusted p value < 0.01; $\log_2$ fold change > 0.4) (Tables S2 and S3, respectively). Given the pronounced movement defects of endophilin mutants, we first looked for movement-disorder-related genes or pathways. Interestingly, TKO versus WT DEGs showed significant enrichment of genes involved in ataxia and PD (Figures 2A and 2B; Table S4).

Because endophilin 1,2 DKO mice present first signs of neurodegeneration by the end of the 2nd postnatal week, hippocampi from DKO, littermate 1KO-2WT, and WT mice were extracted during the 3rd week and subjected to RNA sequencing and transcriptome analysis. The data are again of high technical quality (~28M reads; Table S1; samples clustered well according to genotype; Figures S2D and S2E). 1,479 DEGs between 1,2 DKO and littermate controls, and 1,749 DEGs between DKO and WT were detected (adjusted p value < 0.01; $\log_2$ fold change > 0.4; Tables S5 and S6, respectively). Both 1,2 DKO versus littermate and DKO versus WT lists were significantly enriched for genes involved in ataxia and PD (Table S4; Figures 2C and 2D). Ataxia-related genes include ATM interactor (*Atmin*), *E2f1*, and *Rad51*; PD-related genes include *Park2* (encoding parkin), *Lrrk2*, the tyrosine hydroxylase gene (*Th*), and *Parl*. These findings further support endophilin's association with neurodegeneration, ataxia, and PD (Arranz et al., 2015; Edvardson et al., 2012; Krebs et al., 2013; Matta et al., 2012; Milosevic et al., 2011; Quadri et al., 2013; Ralser et al., 2005; Shi et al., 2009; Trempe et al., 2009).

We next analyzed TKO versus both littermate and WT controls (genes significantly changed in the same direction in TKO against both littermates and WTs; Table S7; Figure S2F) by Ingenuity Pathway Analysis (IPA) software to identify altered pathways and networks. The resulting most-represented pathways were related to compromised synaptic transmission, protein homeostasis, phagosome maturation, mitochondrial function, dopamine metabolism, and apoptosis (Figure 2E). Altered protein homeostasis has been strongly linked to neurodegeneration (e.g., Deger et al., 2015) and might be relevant to the ataxic and neurodegenerative phenotypes observed in endophilin-deficient mice.

The differential expression of several genes was validated by quantitative real-time PCR in endophilin TKO hippocampi versus WT, and a strong correlation was observed ($R^2 = 0.83$; Figure 2F). We also examined regulators of the transcriptional profile in endophilin TKO hippocampi and found that, among those statistically enriched, *Fbxo32* presents the most-robust change in gene expression (1.9-fold increase; Table S8). This was interesting because FBXO32 is an E3-ubiquitin ligase linked to autophagy in skeletal and cardiac muscle (Sandri et al., 2004; Zaglia et al., 2014). Its expression is known to be regulated by the transcription factors FOXO1 and FOXO3A (Sandri et al., 2004; Webb and Brunet, 2014): whereas *Foxo1* was unchanged, *Foxo3a* was significantly upregulated in TKO hippocampi (Table S8).

Absence of Endophilin Upregulates the E3-Ubiquitin Ligase *Fbxo32* and Its Transcription Factor *Foxo3a*

Given the observed changes in the *Foxo3a-Fbxo32* network and that FBXO32 is known to promote cell death and is required for muscle atrophy (Sandri et al., 2004; Wu et al., 2011; Xie et al., 2009), we decided to follow up on this network at the RNA and protein level. As in the RNA-sequencing data, *Foxo3a* and *Fbxo32* were upregulated in TKO hippocampi when measured by qPCR (Figure 3A) whereas *Foxo1* was unchanged (Figures S2G and S2H). A striking increase in FBXO32 protein levels in TKO whole-brain extracts relative to littermate controls and to WT mice was detected (Figure 3B; Figure S2I displays elevated FBXO32 in the hippocampus). Levels of FOXO3A[Ser253] phosphorylation (which represses FOXO3A binding to DNA) were also decreased (Figure 3B), suggesting an increase in the FOXO3A transcriptional activity, and the distribution of FOXO3A[Ser253]-P is altered in TKO hippocampus in comparison to controls (Figure 3C).

To determine whether FOXO3A activation is directly responsible for the upregulation of FBXO32, *Foxo3a* was silenced in TKO primary hippocampal neurons by small interfering RNA (siRNA) knockdown, using two siRNA constructs. Near-complete ablation of FOXO3A affects neuronal survival, so we used a milder condition (45% reduction) to probe for FBXO32 levels (Figure 3D). The elevated FBXO32 levels in TKO neurons were lowered upon *Foxo3a* knockdown, implying that FOXO3A is a sufficient regulator of FBXO32 in this system (Figure 3D). FBXO32 was also strongly upregulated in 1,2 DKO brain samples, both at p0 (whole brain) and 3 weeks (cortex; Figure 3E), as well as in the cortex of 1KO-2HT-3KO mice at 18 months (Figure 3F). Thus, the *Foxo3a-Fbxo32* network originally described in muscle atrophy is operative in the brain of endophilin mutant mice.

Proteasome Saturation in the Absence of Endophilin-A

Given the reported role of FBXO32 in the regulation of protein homeostasis via the UPS, we investigated whether the ubiquitin system is also affected in endophilin mutants. The PD-related E3-ubiquitin ligase parkin monoubiquitinates endophilin, and TKO brains show increased levels of parkin and ubiquitinated proteins (Trempe et al., 2009; Cao et al., 2014). However, 1,2 DKO mice in which the parkin gene *Park2* was also knocked out displayed a similar neurological phenotype to 1,2 DKO mice (Cao et al., 2013), suggesting that other ubiquitin ligases might be involved. Given that FBXO32 is also an E3-ubiquitin ligase, we hypothesized that its robust upregulation in endophilin-deficient brain might contribute to the loss of protein homeostasis in endophilin knockouts. First, we tested whether FBXO32 can (mono)ubiquitinate endophilin-1 and 2, but this was not the case (Figures S3A and S3B). We observed that 1,2 DKO brains also display increased levels of ubiquitinated proteins (Figure 4A), similar to TKO brains (Cao et al., 2013). To distinguish whether this was due to proteasome-related or localization-/signaling-related ubiquitination, we measured K48-(proteasome-related) and K63-(signaling-related)-linkage-specific polyubiquitination (Herhaus and Dikic, 2015). Whereas K48-linked ubiquitination was prominently increased in 1,2 DKO cortical extracts (Figure 4B), there was no significant change in the levels of K63-linked ubiquitination (Figure 4C), suggesting that the accumulation of ubiquitinated proteins is associated with defective processing by the proteasome. A similar result was observed in TKO brains (Figures S3C and S3D).

Given the apparent inability of the proteasome to cope with the level of ubiquitinated proteins in endophilin knockouts, we probed the proteasomal system using a ubiquitinated substrate that is targeted to the proteasome and degraded (ubiquitin-G76V-GFP; Dantuma et al., 2000), as well as by measuring the enzyme activity of the proteasome itself. We observed an accumulation of GFP-fluorescence originating from the substrate in TKO primary hippocampal neurons as well as fibroblasts (mouse embryonic fibroblasts [MEFs]) in comparison to respective controls (Figures 4D and 4E), denoting proteasome saturation in the endophilin KO cells. Interestingly, we noticed that the increase in

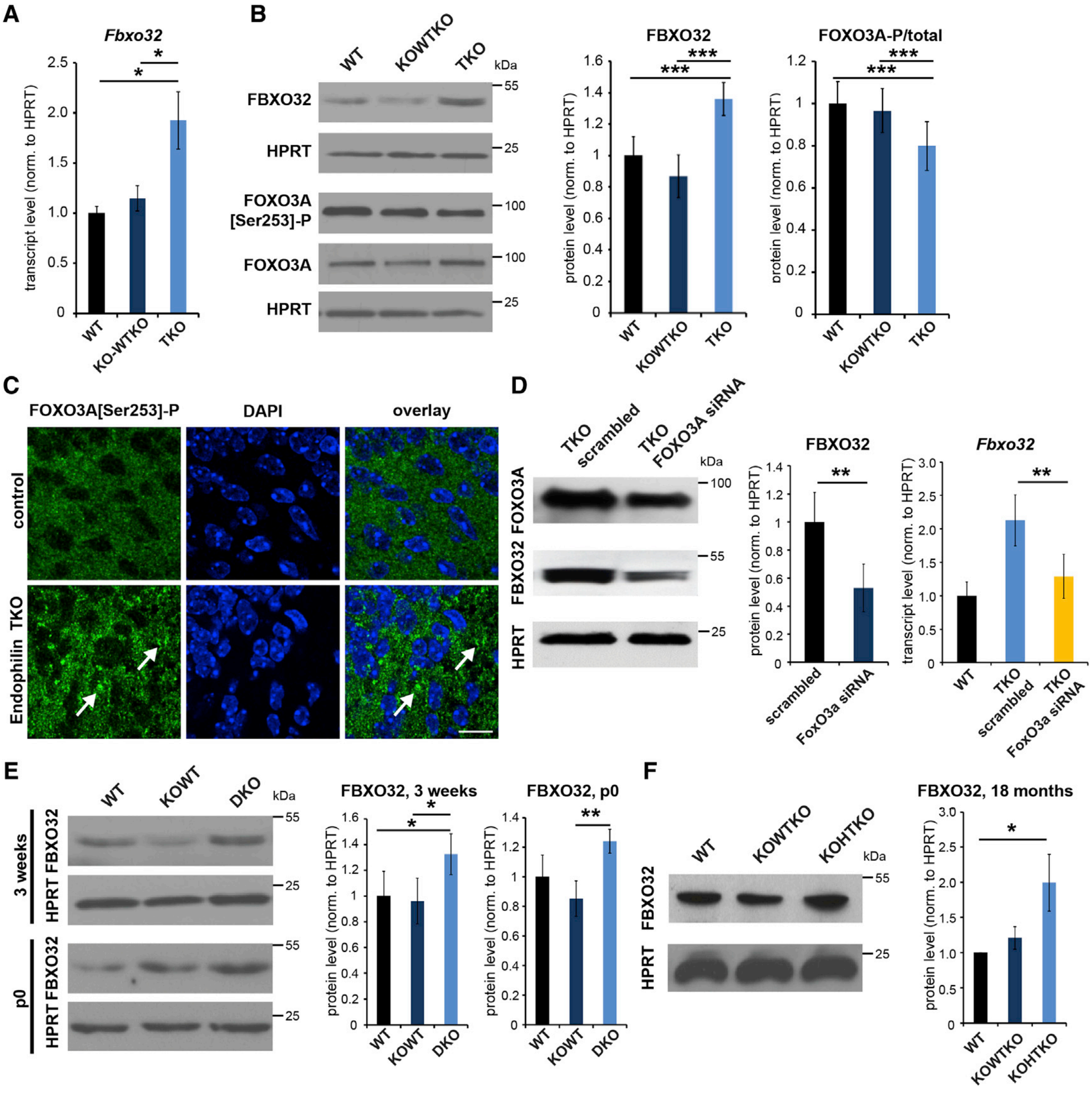

Figure 3. Upregulation of the E3 Ubiquitin Ligase FBXO32 and Its Transcription Factor FOXO3A in Endophilin Mutant Mice

(A) Transcript levels of *Fbxo32* measured by qRT-PCR for indicated genotypes. *$p < 0.05$; Student's t test; mean ± SEM.

(B) Upregulation of FBXO32 and FOXO3A in endophilin TKO whole-brain extracts. (Right) Quantification is shown (min. eight samples/genotype). *$p < 0.05$; ***$p < 0.005$; Student's t test; mean ± SEM.

(C) FOXO3A-[S253]P immunofluorescence reveals its altered distribution (shown by arrows) in brain sections of endophilin TKO hippocampus. Four mice/genotype are shown. The scale bar represents 10 μm.

(D) Silencing TKO neurons with Foxo3a siRNA (left: efficiency of knockdown by western blotting) decreases transcript levels of *Fbxo32* measured by qRT-PCR. n = 3. **$p < 0.01$; Student's t test; mean ± SD.

(E) Upregulation of FBXO32 in endophilin 1,2 DKO brains, at p0 (whole brain) and p14–p21 mice (cortex). (Right) Quantification is shown (eight samples/genotype). *$p < 0.05$; **$p < 0.01$; Student's t test; mean ± SEM.

(F) Upregulation of FBXO32 in endophilin 1KO-2HT-3KO cortical extracts in 18-month mice. (Right) Quantification is shown (three samples/genotype). *$p < 0.05$; Student's t test; mean ± SD.

See also Figures S2 and S3.

ubiquitinated proteins elicited by the expression of ubiquitin-G76V-GFP results in significantly more apoptosis in the TKO MEFs than in controls (Figure 4G). Altogether, these results suggest a causal link between proteasome saturation in endophilin mutants, higher levels of ubiquitinated proteins, and increased cell death susceptibility.

To determine whether the proteasome saturation was due to decreased activity of the proteasome, we measured the proteasome enzyme activity. While there was a trend toward a decrease in proteasomal activity, we observed no significant difference in the proteasome activity per se in the brain extracts (Figure 4F). Thus, the proteasome system in TKO

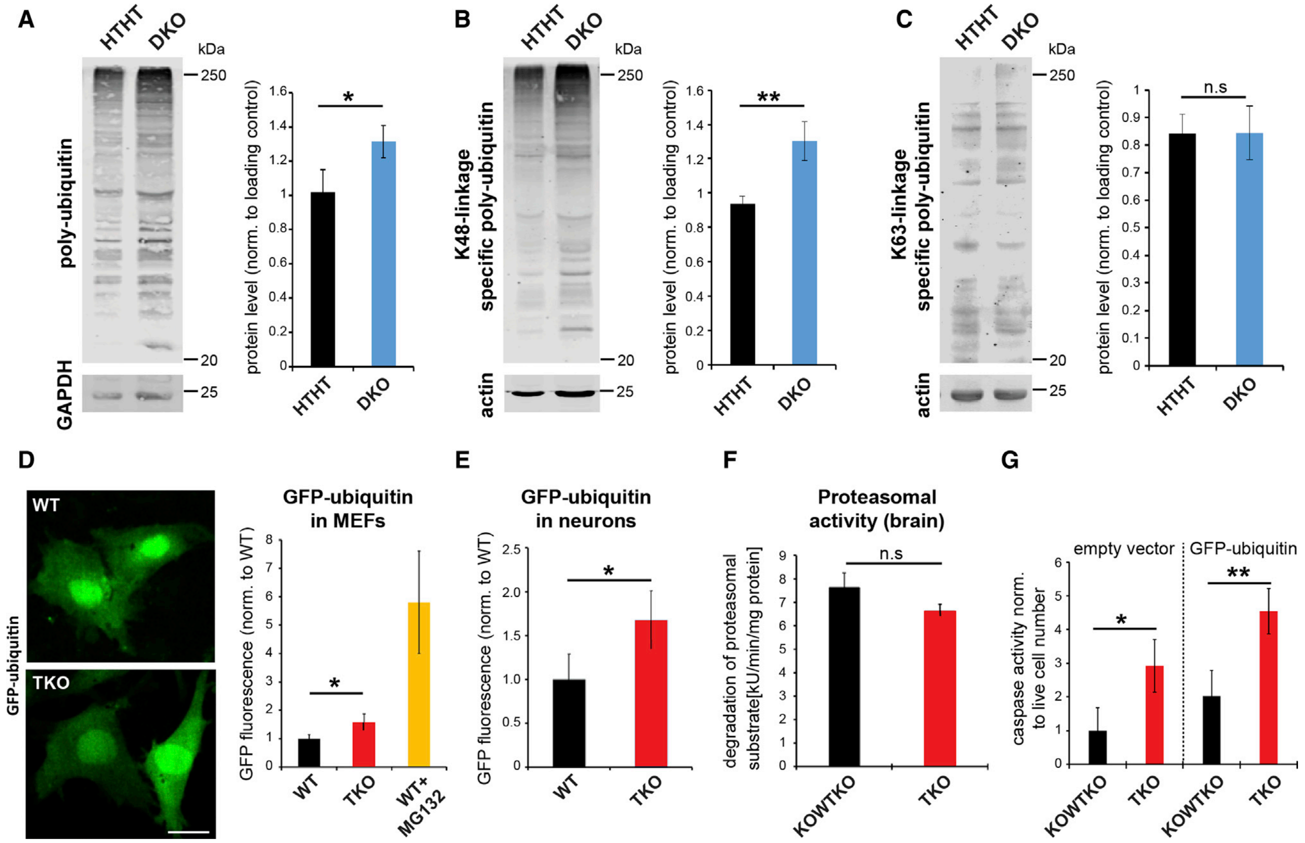

Figure 4. Proteasomal Saturation in Endophilin Mutant Mice

(A–C) Western blots for polyubiquitin (A), K48 linked (B; proteasome targeting), and K63 linked (C; proteasome unrelated) in 1,2 DKO cortex. (Right) Quantification is shown (min. six samples/genotype). $^*p < 0.05$; $^{**}p < 0.01$; Student's t test; mean ± SEM.

(D and E) TKO MEFS (D) or neurons (E) transfected with ubiquitin-G76V-GFP (modified GFP targeted for proteasomal degradation). The scale bar represents 10 μm. (Right) Quantification of GFP fluorescence is shown. In MEFs, proteasome inhibitor MG132 was used as control. $^*p < 0.05$; Student's t test; mean ± SEM.

(F) Proteasomal activity (chymotrypsin-like) in brain extracts of TKOs relative to littermate controls. $p > 0.05$; Student's t test; mean ± SEM.

(G) Activity of caspases 3 and 7 reveals that apoptosis is increased in TKO MEFs transfected with ubiquitin-G76V-GFP. $^{***}p < 0.001$; Student's t test; mean ± SD. See also Figure S3.

brains seems functional but unable to keep up with the high demand.

FBXO32 Interacts with Three Members of the Endophilin-A Family

In light of the upregulation of FBXO32 in the absence of endophilin, we sought to understand the connection between these proteins. First, we tested whether FBXO32 interacts with endophilin family members by immunoprecipitation and pull-downs. An interaction between FBXO32 and all three endophilins in vivo was revealed by specific enrichment of FBXO32 in anti-GFP immunoprecipitates from HeLa expressing FBXO32-mCherry and endophilin 1, 2, or 3-EGFP (Figures 5A–5C). Similar results were obtained by glutathione S-transferase (GST) pull-downs from mouse brain lysate using the GST-FBXO32 as bait (Figure S3E). We demonstrated that FBXO32 is able to pull-down purified endophilin-1 protein (Figure 5D), suggesting a direct interaction. Furthermore, the interaction is mediated through endophilin's SH3 domain, as revealed by another set of pull-downs from mouse brain lysate using the GST-SH3 domains of endophilin-1 and 3 as baits (an enrichment of FBXO32 with stronger binding to endophilin-1 and 3 SH3s was observed; Figure S3F).

We examined the intracellular localization of FBXO32 and its overlap with endophilins in cultured clonal cells (HeLa and MEFs were used to control for cell line variability) and primary hippocampal neurons. It is noteworthy that expressing FBXO32 (either FBXO32-EGFP or FBXO32-mCherry) induced cell death: ~50% of *Fbxo32*-transfected HeLa and ~40% of *Fbxo32*-transfected MEFs survived 30 hr post-transfection; less than 15% of *Fbxo32*-transfected primary neurons were detected on day in vitro (DIV) 14 (detailed below). FBXO32 distribution showed substantial cell-to-cell variability: although mainly cytosolic, FBXO32 was enriched at dynamic organelle-like structures of various sizes and often accumulated in the nucleus (Movie S3). Native FBXO32 distribution was similar to that of expressed FBXO32: immunostaining against FBXO32 revealed nuclear as well as cytosolic protein distribution in HeLa cells (Figure S4A). Surprisingly, both in HeLa cells and MEFs, FBXO32-labeled tubular structures were observed (examples in Figures 5F, 5I, and S4C; see also Movie S5). Given that FBXO32 interacts

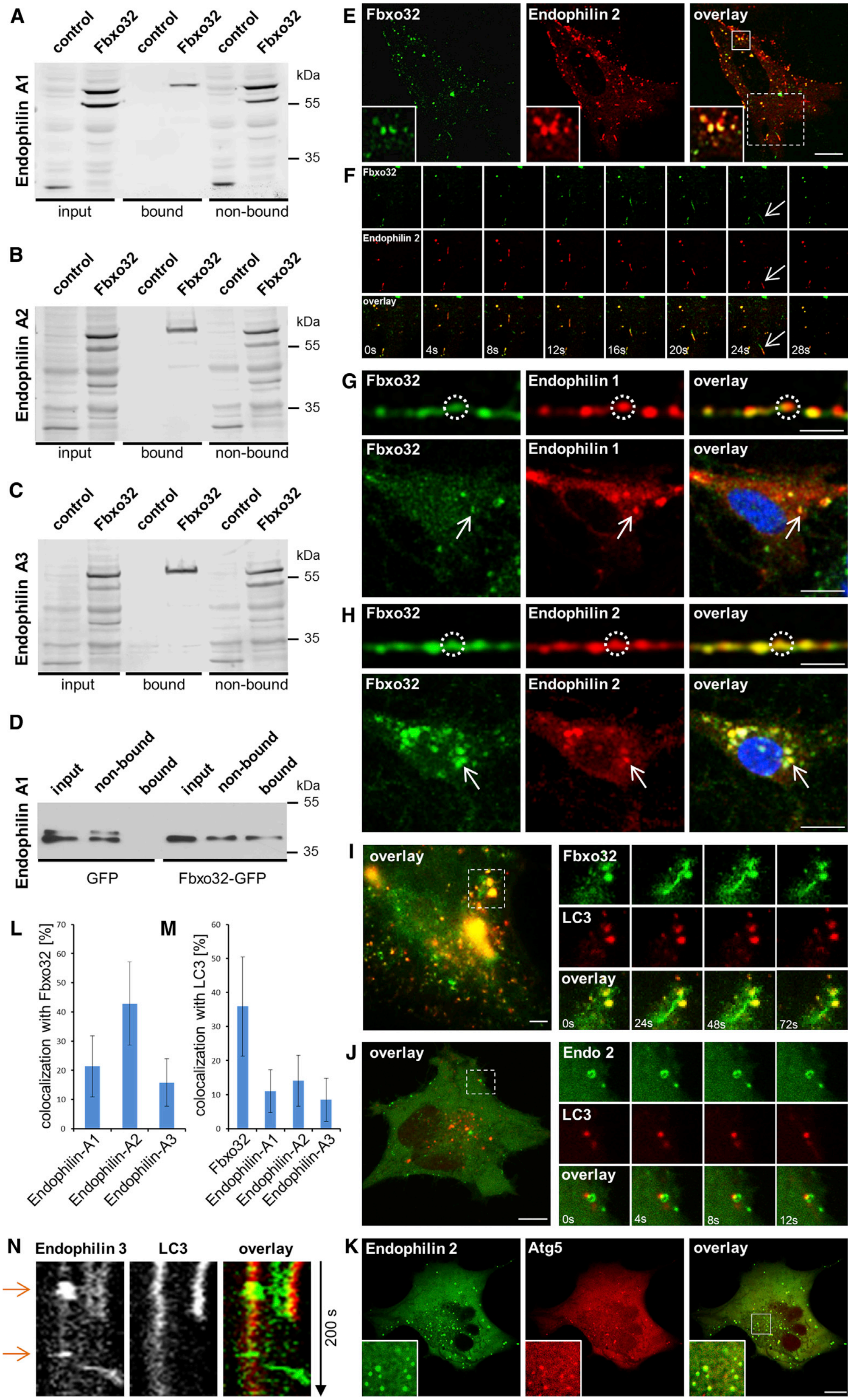

(legend on next page)

with endophilins, and the propensity of endophilins to tubulate membranes, we examined the colocalization of FBXO32 with endophilin 1, 2, and 3. The distribution of endophilins is mainly cytosolic: sparse puncta were attributed to endophilin's role in endocytosis (Milosevic et al., 2011; Perera et al., 2006; Boucrot et al., 2015; Renard et al., 2015).

When endophilin-1 and FBXO32 were coexpressed at similar levels, FBXO32 protein distribution changed: FBXO32 became predominantly cytoplasmic and excluded from the nucleus (Figures S4B and S6E; also see Figures 7B and 7D). Interestingly, we also observed that cell death due to FBXO32 overexpression was abolished upon endophilin coexpression, which we detail further below. FBXO32 and endophilin-1 were also found to colocalize sparsely at dynamic organelle-like structures (Figures 5L and S4B). These were found throughout the cytoplasm and not only in the vicinity of the plasma membrane (as would be expected for endophilin-1 when being recruited to endocytic structures).

When endophilin-2 and FBXO32 were coexpressed, they colocalized transiently at both organelle-like structures and tubuli (Figures 5E, 5L, and S4C; Movie S5). We further observed that endophilin-2 colocalized with FBXO32 on dynamic tubulated structures, although endophilin-2 was not needed for the recruitment of FBXO32 to tubuli (Figure 5F at 24 s; Movie S5). Similarly to endophilins, FBXO32 also directly binds and tubulates membranes in vitro (B. Kroppen, M. Meinecke, and I.M., unpublished data). Lastly, FBXO32 and endophilin-3 colocalized partially on organelle-like structures (Figures 5L and S4D).

We examined the overlap between FBXO32 and endophilin-1 or endophilin-2 in primary hippocampal cultures. FBXO32-EGFP and endophilin-1-mRFP or endophilin-2-mRFP signal overlapped partially both in the cell bodies and in neuronal processes (Figures 5G and 5H; again FBXO32 colocalized to a greater extent with endophilin-2 than endophilin-1).

In sum, the data show that FBXO32 interacts directly with endophilin-A proteins (possibly through their SH3 domain), both proteins are involved in membrane tubulation, and both transiently colocalized on dynamic organelle-like structures of various sizes.

FBXO32 and Endophilins-A Associate Transiently with Autophagosomes

In addition to being an E3-ubiquitin ligase, FBXO32 is known to regulate autophagy in muscle, raising the question of whether the FBXO32-labeled organelle-like structures were autophagosomes. We coexpressed FBXO32-EGFP together with LC3-mRFP and observed a prominent colocalization of the two probes in starved cells (Figures 5I and 5M; Movie S4). A similar result was observed when FBXO32 was immunostained (Figure S4A), irrespective of type of cell (HeLa cells were also used) or fluorescent labeling (Figure S4E). Thus, FBXO32 is detected at autophagosomes.

Next, when endophilin-2 was coexpressed with the autophagosomal marker LC3, sparse but significant colocalization was observed in starved HeLa cells, suggesting that endophilin-2, like FBXO32 albeit to a lesser extent, transiently associates with autophagosomes (Figures 5J and 5M). Similar observations were made for endophilin-1 and endophilin-3, which were also occasionally seen on LC3-labeled autophagosomes (Figures 5M, S4F, and S4G; please note that the values represent colocalization above coincidental colocalization, which is prominent in this system given that endophilins are cytosolic proteins). For example, a kymograph from endophilin-3- and LC3-expressing HeLa cell shows that endophilin-3 colocalizes with an LC3-labeled autophagosome transiently (Figure 5N; arrows indicate colocalization). Importantly, FBXO32, LC3, and endophilin-2 could be simultaneously detected at the same dynamic organelle (Movie S6). Notably, endophilin-2 showed much stronger overlap with ATG5 (an early autophagosomal marker) than with LC3 (Figure 5K; 43% colocalization; see Movie S7), implying a role for endophilin-A in autophagosome formation.

Endophilin-A and FBXO32 Are Needed for Autophagosome Formation in Neurons and in Mammalian Brain

Given that both FBXO32 and endophilins-A were occasionally found on LC3-positive autophagosomes, we examined whether autophagy was altered in brains of TKO and 1,2 DKO mice. Notably, both LC3B-II (lower band is the active form), a classical

---

Figure 5. FBXO32 and Endophilin-A Interact and Colocalize Transiently on Organelles and Tubular Structures

(A–C) Endophilin-1 (A), 2 (B), and 3 (C) interact with FBXO32. Anti-GFP immunoprecipitation from HeLa cell lysate probed with anti-RFP antibody is shown (three experiments).

(D) FBXO32-GFP-coupled beads pull-down purified endophilin-1.

(E) MEF overexpressing FBXO32-EGFP (left) and endophilin A2-RFP (middle); magnified in the inset. Note that FBXO32 and endophilin-2 colocalize on organellar and tubular structures. The scale bar represents 7 μm.

(F) Time-lapse images from (E) showing dynamic tubular structure with FBXO32 and endophilin-2. Note FBXO32's association with membrane tubules independently of endophilin-2. Inset size is 4 μm.

(G and H) Primary hippocampal neurons expressing FBXO32-EGFP and endophilin-1-mRFP (G) or endophilin-2-mRFP (H), transfected by electroporation. (Up) Neuronal processes are shown (scale bar 3 μm). (Bottom) Neuronal cell bodies are shown (scale bar 7 μm).

(I) FBXO32-EGFP colocalization with LC3-mRFP in starved MEF. A representative cell shows the overlay between FBXO32-EGFP and LC3-mRFP (imaged by near-TIRF microscopy). Panels on the right show dynamic FBXO32-labeled tubule. Movie S4 shows trafficking of FBXO32 and LC3 in the same cell. The scale bar represents 3 μm.

(J) HeLa cell expressing LC3-EGFP (left) and endophilin-A2 protein (middle), starved for 2 or 3 hr. The scale bar represents 3 μm.

(K) Endophilin-2-EGFP transiently colocalized with ATG5-mCherry (early autophagosomal marker) in starved HeLa cell. Magnified is shown in the inset. The scale bar represents 5 μm.

(L and M) Quantification of colocalization of endophilins with FBXO32 (L) and LC3 (M). Random colocalization has been subtracted. Mean ± SD.

(N) Kymograph of image series (200 s) showing a transient colocalization of endophilin-3 (green) and LC3 (red) in a HeLa cell imaged by spinning-disk microscopy. See also Figure S4 and Movies S4, S5, S6, and S7.

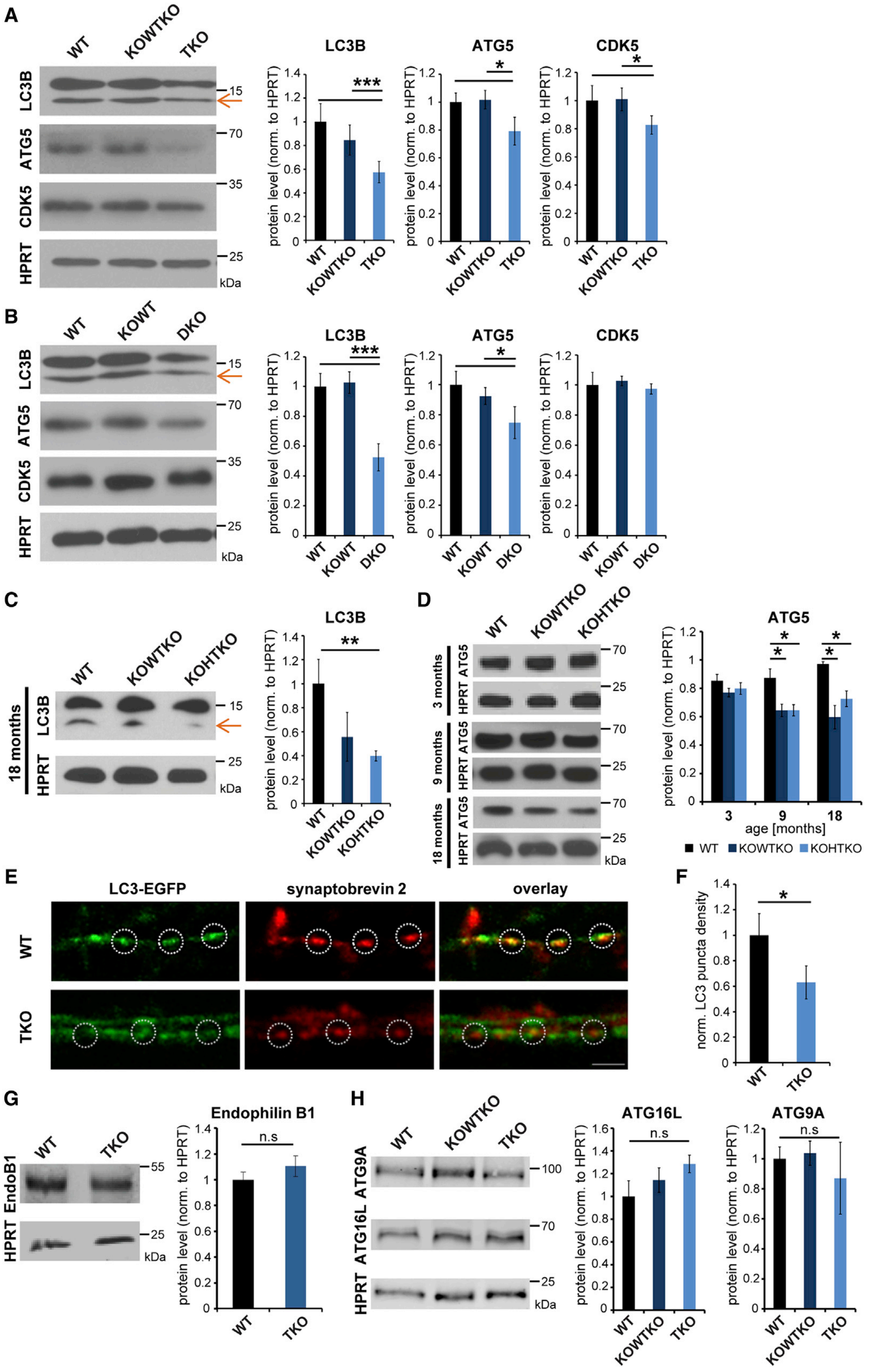

(legend on next page)

marker for autophagosomes, and ATG5, a marker for early autophagosomes, were prominently decreased in TKO brains (Figure 6A) and in aged endophilin 1KO-2HT-3KO mice (Figures 6C and 6D). Interestingly, the ATG5 protein level in endophilin 1KO-2HT-3KO mice decreases progressively between 3 and 18 months of age (Figure 6D). A reduction in LC3B-II and ATG5 was also observed in 1,2 DKO cortex (Figure 6B), suggesting that endophilin-3 cannot effectively compensate for the loss of endophilin-1 and 2 in autophagy.

We prepared primary neuronal cultures from endophilin TKO and WT hippocampi and labeled autophagosomes either by mildly expressing LC3-EGFP (Figures 6E and S5C) or by immunostaining for LC3 (Figure S5E). We detected an overall decrease in the number of LC3-labeled autophagosomes when autophagy was simultaneously induced by starvation and mTOR inhibitor Torin-1 (Figures 6E, 6F, S5C, and S5D). Interestingly, the effect was more obvious at the synapses, as apparent from colocalization of LC3 and synaptobrevin-2, a presynaptic marker (Figure 6E; insets in Figure S5C). Altogether, the biochemical and imaging data suggest that autophagy depends on endophilin in vivo and in vitro and imply a role for endophilin in the formation and/or maturation of autophagosomes.

Notably, endophilin-B has a known role in autophagosome formation, and its CDK5-mediated phosphorylation is required for induced autophagy in models of PD (Wong et al., 2011). Endophilin-A proteins are closely related to endophilin-B: they share an identical domain structure with a high homology, and both protein subfamilies are enriched at the synapses and able to tubulate membranes (Farsad et al., 2001; Ringstad et al., 2001). Thus, we tested the levels of endophilin-B, CDK5, and several autophagy initiators. No change in the protein level of endophilin-B in endophilin-A TKO brains was detected (Figure 6G), whereas the levels of CDK5 were decreased (Figure 6A). However, in 1,2 DKO brains, the CDK5 level was unchanged (Figure 6B). Protein levels of UVRAG, BECLIN, ATG3, and HDAC6 were not altered, either in endophilin TKO brains or endophilin 1,2 DKO cortex (Figures S5A and S5B). These results imply that endophilin-B cannot compensate for autophagosome formation in the absence of endophilin-A and that autophagy is not altered due to repression of signaling pathways, because the key autophagy initiation regulators are not affected by absence of endophilin-A.

The key autophagy factors ATG9A and ATG16L have been shown to undergo clathrin-mediated endocytosis (Ravikumar et al., 2010a; Puri et al., 2014). In the light of endophilins' well-established role in endocytosis, it is possible that the observed phenotype is an indirect effect of defective endocytosis in endophilin mutants. However, we found that both ATG9A and ATG16L were not significantly changed in our mutants (Figures 6H and S5F), indicating that availability of these two factors does not influence the findings we describe here.

To further characterize the role of FBXO32 in autophagy, we employed the *Drosophila melanogaster* neuromuscular junction (NMJ) to see whether FBXO32 is relevant for autophagy in neuronal cells in vivo. When *Fbxo32* is silenced in *Drosophila* in vivo, there was a very obvious decrease in the number of autophagosomes detected at the NMJ (Figures S6A–S6C; quantification in Figure S6D). Thus, FBXO32 seems necessary for autophagosome formation at the fruit fly NMJ.

Given that, in the endophilin mutant brains there is more FBXO32 and yet still less autophagosome formation, the interaction between endophilin and FBXO32 may play a key role in this process.

Fbxo32 Upregulation Causes Apoptosis in Cells and Neurons that Can Be Rescued by Endophilin-A

To determine whether upregulation of *Fbxo32* is an important step in the brain pathology of endophilin mutants, we explored the consequences of *Fbxo32* upregulation in clonal (HeLa and MEF) and primary (neurons) cell lines. It has been reported that FBXO32 elevation induces apoptosis in cardiomyocytes and cancer cells (Wu et al., 2011; Xie et al., 2009). We observed that expression of FBXO32 causes substantial cell death in HeLa and MEFs, as determined by the number of remaining EGFP-positive cells and by the activity of caspases 3 and 7 (Figures 7A–7C, 7E, and S6E). The remaining cells looked unhealthy: they were smaller and often had vacuolar structures. The detrimental effects of FBXO32 were independent of its fluorescent tag and cell-transfection method (electroporation/Lipofectamine/Fugene).

Strikingly, when endophilin-1 was coexpressed with FBXO32 in MEFs, FBXO32-induced cell death was rescued, as demonstrated by the number of EGFP-positive cells (normalized [norm.] to total DAPI count) 30 hr after transfection and healthy cell appearance (Figure 7B; also in HeLa cells: Figure S6E), the quantification of cell survival (Figure 7C), and the activity of caspases 3 and 7 (Figure 7E). Importantly, the levels of FBXO32 expression were elevated when FBXO32 and endophilin-1 were coexpressed, implying that the rescue of FBXO32-induced

Figure 6. Number of Autophagosomes Is Decreased in Endophilin TKO and 1,2 DKO Mutant Brains and Neurons

(A and B) Decrease in autophagosomal markers LC3B-II, ATG5, and CDK5 in TKO brain (A; p0) or 1,2 DKO cortical extracts (B; p14–p21). (Right) Quantification is shown (min. six samples/genotype). $^{*}p < 0.05$; $^{***}p < 0.001$; Student's t test; mean ± SEM.

(C) Decrease in the autophagosomal marker LC3B-II in the cortex of aged endophilin 1KO-2HT-3KO mice. (Right) Quantification is shown (three cortices/genotype). $^{**}p < 0.01$; Student's t test; mean ± SEM.

(D) Decrease in the early autophagosomal marker ATG5 in the cortex of 3-, 9-, and 18-month-old endophilin 1KO-2HT-3KO mice. (Right) Quantification is shown (min. three samples/genotype). $^{*}p < 0.05$; Student's t test; mean ± SEM.

(E) Endophilin TKO and control hippocampal neurons transfected with LC3-EGFP and treated with 250 nM Torin-1 in the EBSS buffer for 4 hr were co-stained for synaptobrevin-2. Note that less LC3 signal can be detected at TKO synapses when compared to WTs (circles indicate synapses). Also note weaker synaptobrevin-2 staining in TKO samples is shown, in agreement with Milosevic et al. (2011). The scale bar represents 2 μm.

(F) Quantification of LC3 puncta in (C). $^{*}p < 0.05$; t test; mean ± SEM.

(G) Endophilin-B1 in TKO brains. (Right) Quantification is shown (eight samples/genotype); mean ± SEM.

(H) Autophagosomal markers ATG9A and ATG16L are not changed in endophilin TKO brains (p0). (Right) Quantification is shown (min. four samples/genotype). $^{*}p < 0.05$; $^{***}p < 0.001$; Student's t test; mean ± SEM.

See also Figure S5.

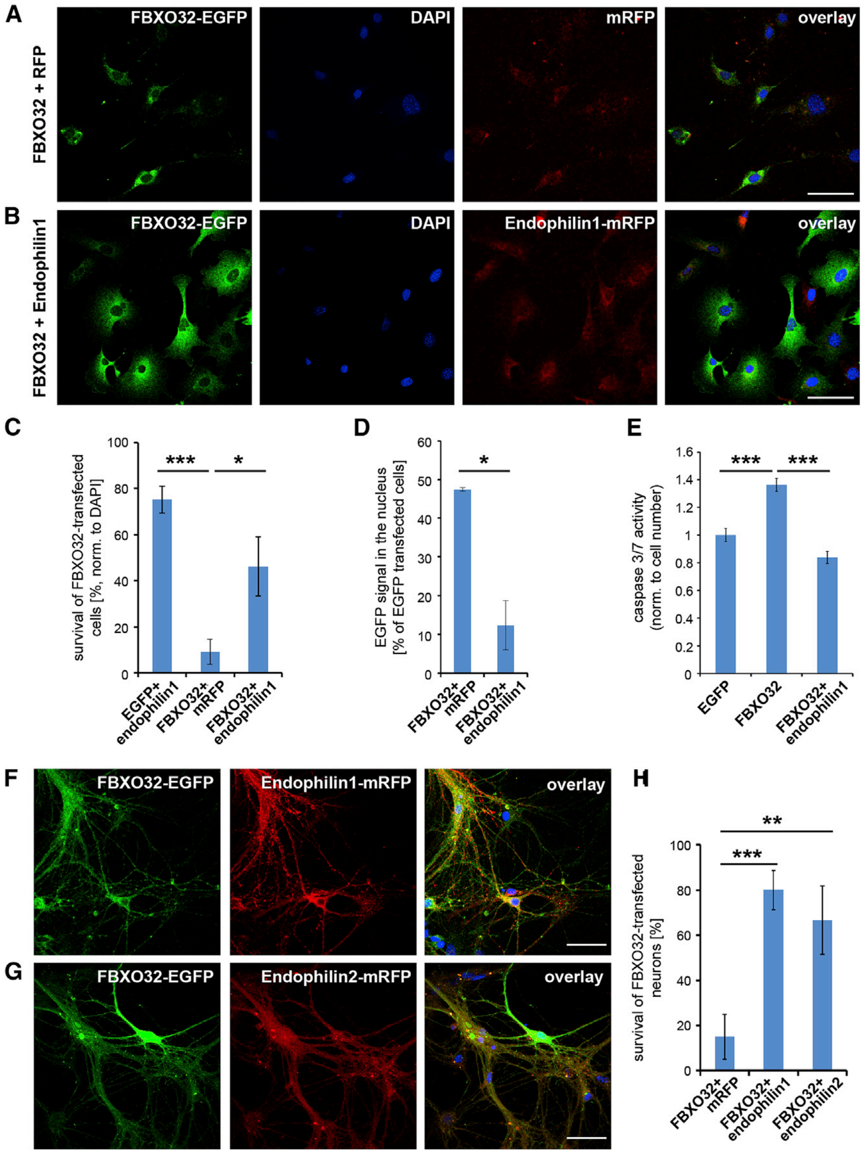

Figure 7. FBXO32 Upregulation Causes Apoptosis in Non-neuronal and Neuronal Cells that Can Be Rescued by Endophilin-1 and 2

(A and B) MEFs cotransfected with FBXO32-EGFP and mRFP (A) or EGFP and endophilin-1-mRFP (B) for 30 hr. Note that FBXO32-expressing cells look healthy if coexpressing endophilin-1. The scale bar represents 20 μm.

(C) Quantification of EGFP-positive cells in (A) and (B) normalized to DAPI. Three experiments are shown, with at least 48 cells/condition. ***$p < 0.001$; *$p < 0.05$. Student's t test; mean ± SEM.

(D) Quantification of EGFP signal in the nucleus in (A) and (B) normalized to total transfected cells. *$p < 0.05$; Student's t test.

(E) Activity of caspases 3 and 7 reveals that apoptosis is increased upon *Fbxo32* expression but abolished when cells coexpress endophilin-1 (three experiments). ***$p < 0.001$; Student's t test; mean ± SEM.

(F and G) Primary cortical neurons cotransfected with FBXO32-EGFP and endophilin-1-mRFP (F) or endophilin-2-mRFP (G). The scale bar represents 20 μm.

(H) Quantification of survival of FBXO32-transfected neurons in primary culture (as shown in F and G; three independent experiments). **$p < 0.01$; ***$p < 0.001$; Student's t test, mean ± SD.

See also Figure S6.

apoptosis is not due to a reduction in FBXO32 levels (Figures 7A and 7B). However, coexpression with endophilin-1 seemed to relocate FBXO32-EGFP out of the nucleus (Figures 7D and S6E) in agreement with the data presented in Figure 5. Thus, FBXO32-induced apoptosis is associated with aberrant intracellular FBXO32 localization, and both the localization and the apoptosis susceptibility can be rescued by simultaneous upregulation of endophilin-1. These data show that FBXO32 and endophilin-1 interact not only at the protein but also at the genetic level.

In neurons, the effect was even more striking. When either WT primary hippocampal or cortical neurons were transfected with FBXO32-EGFP, less than 15% of all transfected neurons were detected at DIV14 (Figures 7F–7H). The surviving FBXO32-expressing neurons displayed a lower number of processes and appeared unhealthy (Figure S6F). TKO hippocampal and cortical neurons in culture were comparable to WT and littermate endophilin 1KO-2WT-3KO cells and did not show increased cell death under standard culturing conditions. However, when TKO cortical neurons were transfected with *Fbxo32*, less than 2% of transfected neurons were detected at DIV14 (in comparison to EGFP-expressing TKO neurons), with the surviving cells presenting a reduction in the number of processes and vacuoles in cell bodies. Lastly, coexpression of endophilin-1 or endophilin-2 was able to rescue FBXO32-induced apoptosis in cortical neurons: when endophilin-1-mRFP or endophilin-2-mRFP were coexpressed with FBXO32-EGFP, either in WT and endophilin TKO cortical neurons, the majority of neurons thrived (over 80% and 67% of all *Fbxo32*-transfected neurons, respectively; Figures 7F–7H). Imbalance in FBXO32/endophilin-A levels is likely a key mechanistic step in the brain pathology of endophilin mutants, and FBXO32-endophilin interplay seems important for maintaining neuronal health and overall protein homeostasis in the brain.

DISCUSSION

To date, the known roles of endophilin-A have been limited to endocytosis and SV recycling. Here, we show that endophilin also affects the UPS and autophagy in the brain. The robust induction of the *Foxo3a/Fbxo32* network (known to mediate muscle atrophy) in the brain of mice with endophilin deficiency promotes apoptosis and likely mediates brain pathology. Similarly to muscle, the *Foxo/Fbxo32* network seems relevant for regulating protein degradation in the brain and for maintaining neuronal health. If FBXO32 is expressed in cell lines and primary neurons, it causes apoptosis that can be rescued by simultaneous coexpression of endophilin. Thus, balancing the FBXO32-endophilin interaction seems essential for sustaining neuronal viability.

We also report that partial endophilin absence in mice results in neurodegeneration and in perturbations of a significant number of ataxia- and PD-related genes. These observations corroborate a number of recent findings that indirectly link endophilin to neurodegeneration and PD (Arranz et al., 2015; Edvardson et al., 2012; Krebs et al., 2013; Matta et al., 2012; Milosevic et al., 2011; Quadri et al., 2013; Shi et al., 2009; Trempe et al., 2009). Endophilin models may also be of relevance for neurodegeneration research because they may provide insights into signaling pathways affected prior to overt manifestation of neurodegeneration.

FBXO32 was thus far studied mainly in skeletal muscle, where this E3-ubiquitin ligase was found to mediate rapid atrophy as a result of FOXO3A transcriptional activation. Interestingly, FOXO3A activation is associated with cellular stress responses and neurodegeneration (Webb and Brunet, 2014). FOXO3A stimulates autophagy in neurons (Xu et al., 2011), and FBXO32 is necessary for autophagy; activation of the *FoxO-Fbxo32* axis should thus lead to increased autophagy. Nevertheless, this is not the case when endophilin is lacking: the number of autophagosomes is sharply decreased. Also, endophilin colocalizes transiently with mature and even more impressively with early autophagosomes, suggesting that endophilin-A has a previously unreported role in the formation and/or maturation of autophagosomes. This is supported by the recent identification of endophilin-A as one of the regulators of autophagosome formation (Strohecker et al., 2015). Interestingly, mice without endophilin also display the same pattern of perinatal lethality observed in mice lacking proteins necessary for autophagosome formation (Kuma et al., 2004).

Given endophilin's involvement in endocytic processes, the decrease in the number of autophagosomes might also result from compromised endocytosis. Specifically, it has been shown that blockage of endocytosis upstream of clathrin coat assembly results in decreased autophagosome formation (Ravikumar et al., 2010a, 2010b). However, endophilin deficiency results in the accumulation of clathrin-coated vesicles, and the levels of clathrin are not altered (Milosevic et al., 2011). Thus, clathrin is available to interact with ATG16L1, and RNA and protein levels of ATG16L1 are not altered in this model. In addition, the RNA and protein levels of ATG9, a key autophagic protein known to traffic via the plasma membrane and endosomal compartments (Mari et al., 2010; Puri et al., 2014) are not altered in endophilin mutant brains. Altogether, whereas we cannot entirely exclude endophilin's role in endocytosis also affecting autophagy, we consider other mechanism(s) besides endocytic defects to be underlying the decrease in autophagosomes in endophilin mutants.

Decreased autophagosome availability and, consequently, lower autophagic flux are known to affect protein homeostasis (Korolchuk et al., 2009). We observed an accumulation of K48-linked ubiquitinated proteins in the cytoplasm, suggesting saturation of the UPS (due to overloading rather than deficiencies in the proteasome). There is possibly a double hit on this pathway: decreased autophagy and increased availability of ubiquitin ligases (FBXO32 and parkin). Both FBXO32 and parkin are involved in selective autophagy of ubiquitinated proteins (Zaglia et al., 2014), and both function under the regulation of FOXOs (Webb and Brunet, 2014). Upregulation of FBXO32 and parkin may thus be a compensatory response to defective autophagy, an attempt to shunt more of the burden to the UPS, or possibly both.

Interestingly, the lower abundance of autophagosomes in the absence of endophilin-A cannot be (fully) compensated for by a related protein with the same domain organization, endophilin-B, an established mediator of autophagosome formation (Takahashi et al., 2011). Endophilin-A primarily operates in the endocytic processes at the plasma membrane, whereas endophilin-B has prominent roles in apoptosis, mitochondrial membrane dynamics, and autophagosome formation (Kjaerulff et al., 2011). Furthermore, CDK5-mediated phosphorylation of endophilin-B is required for inducing autophagy in models of PD (Wong et al., 2011). More research is needed to understand endophilin-A and endophilin-B links to autophagy, neurodegeneration, and PD.

We propose a model in which endophilin's absence, likely due to its membrane-curvature-inducing/stabilizing properties, leads to reduced availability of membranes for autophagosome formation and decreased autophagic activity. Interestingly, FBXO32 and endophilin interact at both the gene and protein level and both are required for the autophagy process. Like endophilin, FBXO32 can tubulate membranes and is recruited to membrane tubules in vivo. Thus, endophilin and FBXO32 membrane-tubulating activity may contribute to the formation/maturation of autophagosomes. This model is in concordance with the reported role of endophilin-A as necessary and sufficient for macroautophagy at presynaptic terminals of fruit flies (Soukup et al., 2016).

In summary, our study addresses the origin of neurodegeneration in a key mammalian endocytic model and reveals that the FOXO/FBXO32/endophilin network may play a role in maintaining neuronal health by balancing autophagy and the UPS in the brain. The results are consistent with the following plausible scenario: reduced endophilin availability results in impaired capacity to form autophagosomes, resulting in decreased autophagy, accumulation of ubiquitinated proteins in the cytoplasm, proteasome saturation, and further accumulation of unwanted proteins over time that eventually affect neuronal function and health, leading to neurodegeneration. Accordingly, we show that imbalanced autophagy also develops in aged endophilin heterozygote mice that display age-dependent progressive ataxia. Our data reveal a role in autophagy for a key endocytic adaptor previously thought to be strictly dedicated to endocytosis and invite further research addressing the physiological and pathological implications of these findings.

EXPERIMENTAL PROCEDURES

Reagents and Gene-Targeting Strategies

Unless otherwise stated, reagents were purchased from Sigma-Aldrich. Supplemental Experimental Procedures detail gene-targeting and cloning strategies and list the antibodies and plasmids used.

Behavior Experiments

Animal experiments were conducted according to the European Guidelines for animal welfare (2010/63/EU) with approval by the Lower Saxony Landesamt für Verbraucherschutz und Lebensmittelsicherheit (LAVES), registration number 14/1701.

For rotarod experiments, 6–20 males/group were tested on a setup by TSE Systems (3375-5). A training phase consisted of four trainings over 2 days (intertrial interval [ITI] was 2–5 hr; 180 s at 5 rpm). The testing phase consisted of four tests over 2 days (ITI 2–5 hr). Mice were placed on the rod, which then accelerated from 5 to 40 rpm in 180 s. Fall latency was measured. Student's t test was applied.

A simple composite phenotype scoring system for evaluating mouse models of ataxia was applied as described (Guyenet et al., 2010). Eight to twelve mice were used per condition, and scoring was performed by two researchers independently. Data were analyzed using two-way ANOVA.

Ventral plane videography for gait analysis was performed using instrumentation (DigiGait) and software from Mouse Specifics, according to manufacturer's instructions. For each group, 6–20 males were used. Student's t test was applied.

Fluorescence Imaging

TUNEL assay was performed on cryosections of the brains of perfused mice to test for apoptotic and necrotic cells. Mice were anesthetized with chloral hydrate (40 mg/mL) before cardiac perfusion with 4% paraformaldehyde (PFA). Harvested brains were post-fixed in PFA. After slow dehydration with sucrose, brains were embedded in OCT (Tissue Tek) and frozen in liquid N_2. Sagittal brain sections were cut with a cryostat (10 μm thick). Sections were post-fixed and permeabilized with 0.1% Triton X-100. Positive controls were incubated with DNase I (833 U/mL). In Situ Cell Death Detection Kit (Fluorescein) was used according to manufacturer's instructions. Slides were counterstained with DAPI, embedded with Mowiol 4-88, and imaged with a LSM 710 confocal setup (Zeiss). Immunofluorescence of frozen brain sections and cultured neurons (DIV 14–20) was carried out as described (Ringstad et al., 2001; Milosevic et al., 2011). Live MEFs, HeLa cells, and neurons were imaged either using a Zeiss AxioObserver Z1 total internal reflection fluorescence (TIRF) microscope with an Evolve charge-coupled device (CCD) camera (Photometrics) and 100× Plan Apo Zeiss objective or Perkin Elmer Ultraview spinning-disk confocal setup that consists of Nikon Ti-E Eclipse inverted microscope equipped with Perfect Focus, 60× CFI Plan Apo VC Nikon objective, and 14-bit electron-multiplied CCD camera (Hamamatsu C9100). Autophagy induction and colocalization analysis was performed as detailed in the Supplemental Experimental Procedures and below.

RNA Sequencing

RNA sequencing was performed as described in Halder et al. (2016). The pathway analysis was performed as described in Raimundo et al. (2012). These methods are detailed in Supplemental Experimental Procedures.

Biochemical Procedures

Whole-brain or cortex samples for western blotting were prepared by homogenization of brain tissue (whole brain for p0 animals; one cortex for p14–p21 animals and aged animals) as detailed in Supplemental Experimental Procedures. For Trap-GFP immunoprecipitation, HeLa cells were transfected with endophilin (1, 2, or 3)-EGFP and mCherry/FBXO32-mCherry using Lipofectamine 3000 (Invitrogen). We used Chromotek Trap-GFP agarose beads (Chromotek) and followed manufacturer's protocol. Alternatively, HeLa cells were transfected with FBXO32-EGFP and coupled to Chromotek Trap-GFP agarose beads. Purified endophilin-1 was added, and all fractions (input, non-bound, and bound) were collected. Samples were subjected to SDS-PAGE electrophoresis and immunoblotted against indicated proteins.

Cell Culture

siRNA-based knockdown of *Foxo3a* was performed as in Milosevic et al. (2011). Primary hippocampal and cortical cultures were prepared as previously described (Ferguson et al., 2007). Primary neurons expressed constructs, following Amaxa (Lonza)-based transfection, under the control of the chicken-β-actin promoter to allow for long-term expression. A minimum of 15 images from three to five experiments were analyzed for each genotype/condition. Given that the majority of respective fluorescent signals were cytosolic, colocalization was evaluated semi-automatically using object-based overlap analysis and ImageJ JACoP plugin (Bolte and Cordelières, 2006). In short, the image was first segmented into objects and background (i.e., bright fluorescent objects are segmented from the image), and then their spatial relationship (overlap) was measured. The same analysis was performed with the mirror image, and random colocalization was subtracted in each case. Complementary manual colocalization analysis was also performed, and it yielded similar results. Here, circles were superimposed on bright fluorescent spots in the FBXO32 (or LC3 or ATG5) channel and transferred to identical image locations in the endophilin channel. If the fluorescence intensity maximum in the endophilin channel was located in the same circle and the morphology of the signal resembled that of the FBXO32 signal, the circle was rated as positive (colocalized); if not, it was rated as negative (not colocalized). To correct for accidental colocalization, circles were also transferred to a mirror image of the endophilin channel (detailed in Supplemental Experimental Procedures). Fluorescent puncta were quantified as in Hayashi et al. (2008). Data are presented as puncta per 100 μm^2, normalized to controls. Student's t test was used unless otherwise stated.

Proteasome Activity Assay

We used WT and endophilin TKO MEFs, immortalized with E6/E7 viral proteins, grown on supplemented DMEM at 5% CO_2 at 37°C. The cells were about 70%–80% confluent when harvested. Cells were pelleted and resuspended with n-dodecylmaltoside 1.5% in PBS with Complete Protease Inhibitor Cocktail (Roche) and PhosSTOP phosphatase inhibitor cocktail (Roche) and lysed at 4°C in a rotator for 30 min. The lysate was then centrifuged to pellet debris and placed in 96-well glass-bottomed plates for use in the assay. The fluorimetric proteasome assay (Proteasome 20S Activity Assay Kit) was performed according to manufacturer's instructions using a Synergy H1 plate reader (Biotek) at 37°C.

Caspase Activity Assay

Caspase 3/7 apoptosis assay was performed with the ApoTox-Glo Triplex Assay (Promega) kit according to a modified version of the manufacturer's protocol for 96-well plates, detailed in Supplemental Experimental Procedures.

ACCESSION NUMBERS

The accession number for the NGS data reported in this paper is GEO: GSE85702.

SUPPLEMENTAL INFORMATION

Supplemental Information includes Supplemental Experimental Procedures, six figures, eight tables, and seven movies and can be found with this article online at http://dx.doi.org/10.1016/j.celrep.2016.09.058.

AUTHOR CONTRIBUTIONS

Conceptualization, N.R. and I.M.; Methodology, J.D.M., N.R., and I.M.; Resources, P.V., S.B., A.F., N.R., and I.M.; Investigation and Analysis, J.D.M., C.M.R., S.G., A.S.A., S.F.S., S.F., R.V., V.C., P.V., S.B., N.R., and I.M. (J.D.M.: Figures 2E [with N.R.], 3A, 3B, 3E, and 6A–6C; C.M.R.: Figures 1 [with I.M.], 3C, 3F, 4A–4C, 6D, 6G, and 6H); Supervision, P.V., S.B., N.R., and I.M.; Writing – Original Draft, J.D.M., N.R., and I.M.; Writing – Review & Editing, C.M.R., J.D.M., N.R., and I.M.

ACKNOWLEDGMENTS

We thank M. König, E. Rizou, J. Liebig, and S. Burkhardt for superb technical assistance; A. Cepeda for help with protein expression and purification; B. Flix for cloning; and J. Kroll for video processing. This work was supported in part by grants from Schram-Stiftung T287/25457 and Deutsche Forschungsgemeinschaft (DFG) (Emmy Noether Young Investigator Award MI 1702/1 and SFB889/2/A08) to I.M., ERC Starting Grant 337327 to N.R., an Alexander von Humboldt postdoctoral fellowship to J.D.M., and a SySy fellowship to S.G.

Received: March 11, 2016
Revised: June 24, 2016
Accepted: September 19, 2016
Published: October 6, 2016

REFERENCES

Arranz, A.M., Delbroek, L., Van Kolen, K., Guimarães, M.R., Mandemakers, W., Daneels, G., Matta, S., Calafate, S., Shaban, H., Baatsen, P., et al. (2015). LRRK2 functions in synaptic vesicle endocytosis through a kinase-dependent mechanism. J. Cell Sci. *128*, 541–552.

Bolte, S., and Cordelières, F.P. (2006). A guided tour into subcellular colocalization analysis in light microscopy. J. Microsc. *224*, 213–232.

Boucrot, E., Ferreira, A.P., Almeida-Souza, L., Debard, S., Vallis, Y., Howard, G., Bertot, L., Sauvonnet, N., and McMahon, H.T. (2015). Endophilin marks and controls a clathrin-independent endocytic pathway. Nature *517*, 460–465.

Cao, M., Milosevic, I., Giovedi, S., and De Camilli, P. (2013). Genetic interaction between endophilin and Parkin. In Society for Neuroscience (SfN) Annual Meeting 2013, p. 423.12.

Cao, M., Milosevic, I., Giovedi, S., and De Camilli, P. (2014). Upregulation of Parkin in endophilin mutant mice. J. Neurosci. *34*, 16544–16549.

Cookson, M.R. (2010). The role of leucine-rich repeat kinase 2 (LRRK2) in Parkinson's disease. Nat. Rev. Neurosci. *11*, 791–797.

Dantuma, N.P., Lindsten, K., Glas, R., Jellne, M., and Masucci, M.G. (2000). Short-lived green fluorescent proteins for quantifying ubiquitin/proteasome-dependent proteolysis in living cells. Nat. Biotechnol. *18*, 538–543.

Deger, J.M., Gerson, J.E., and Kayed, R. (2015). The interrelationship of proteasome impairment and oligomeric intermediates in neurodegeneration. Aging Cell *14*, 715–724.

Edvardson, S., Cinnamon, Y., Ta-Shma, A., Shaag, A., Yim, Y.I., Zenvirt, S., Jalas, C., Lesage, S., Brice, A., Taraboulos, A., et al. (2012). A deleterious mutation in DNAJC6 encoding the neuronal-specific clathrin-uncoating co-chaperone auxilin, is associated with juvenile parkinsonism. PLoS ONE *7*, e36458.

Esposito, G., Ana Clara, F., and Verstreken, P. (2012). Synaptic vesicle trafficking and Parkinson's disease. Dev. Neurobiol. *72*, 134–144.

Farsad, K., Ringstad, N., Takei, K., Floyd, S.R., Rose, K., and De Camilli, P. (2001). Generation of high curvature membranes mediated by direct endophilin bilayer interactions. J. Cell Biol. *155*, 193–200.

Ferguson, S.M., Brasnjo, G., Hayashi, M., Wölfel, M., Collesi, C., Giovedi, S., Raimondi, A., Gong, L.W., Ariel, P., Paradise, S., et al. (2007). A selective activity-dependent requirement for dynamin 1 in synaptic vesicle endocytosis. Science *316*, 570–574.

Guyenet, S.J., Furrer, S.A., Damian, V.M., Baughan, T.D., La Spada, A.R., and Garden, G.A. (2010). A simple composite phenotype scoring system for evaluating mouse models of cerebellar ataxia. J. Vis. Exp. (*39*), 1787.

Halder, R., Hennion, M., Vidal, R.O., Shomroni, O., Rahman, R.U., Rajput, A., Centeno, T.P., van Bebber, F., Capece, V., Garcia Vizcaino, J.C., et al. (2016). DNA methylation changes in plasticity genes accompany the formation and maintenance of memory. Nat. Neurosci. *19*, 102–110.

Hayashi, M., Raimondi, A., O'Toole, E., Paradise, S., Collesi, C., Cremona, O., Ferguson, S.M., and De Camilli, P. (2008). Cell- and stimulus-dependent heterogeneity of synaptic vesicle endocytic recycling mechanisms revealed by studies of dynamin 1-null neurons. Proc. Natl. Acad. Sci. USA *105*, 2175–2180.

Herhaus, L., and Dikic, I. (2015). Expanding the ubiquitin code through post-translational modification. EMBO Rep. *16*, 1071–1083.

Heutink, P., and Verhage, M. (2012). Neurodegeneration: new road leads back to the synapse. Neuron *75*, 935–938.

Iaccarino, C., Crosio, C., Vitale, C., Sanna, G., Carrì, M.T., and Barone, P. (2007). Apoptotic mechanisms in mutant LRRK2-mediated cell death. Hum. Mol. Genet. *16*, 1319–1326.

Kjaerulff, O., Brodin, L., and Jung, A. (2011). The structure and function of endophilin proteins. Cell Biochem. Biophys. *60*, 137–154.

Korolchuk, V.I., Mansilla, A., Menzies, F.M., and Rubinsztein, D.C. (2009). Autophagy inhibition compromises degradation of ubiquitin-proteasome pathway substrates. Mol. Cell *33*, 517–527.

Krebs, C.E., Karkheiran, S., Powell, J.C., Cao, M., Makarov, V., Darvish, H., Di Paolo, G., Walker, R.H., Shahidi, G.A., Buxbaum, J.D., et al. (2013). The Sac1 domain of SYNJ1 identified mutated in a family with early-onset progressive Parkinsonism with generalized seizures. Hum. Mutat. *34*, 1200–1207.

Kuma, A., Hatano, M., Matsui, M., Yamamoto, A., Nakaya, H., Yoshimori, T., Ohsumi, Y., Tokuhisa, T., and Mizushima, N. (2004). The role of autophagy during the early neonatal starvation period. Nature *432*, 1032–1036.

Mari, M., Griffith, J., Rieter, E., Krishnappa, L., Klionsky, D.J., and Reggiori, F. (2010). An Atg9-containing compartment that functions in the early steps of autophagosome biogenesis. J. Cell Biol. *190*, 1005–1022.

Matta, S., Van Kolen, K., da Cunha, R., van den Bogaart, G., Mandemakers, W., Miskiewicz, K., De Bock, P.J., Morais, V.A., Vilain, S., Haddad, D., et al. (2012). LRRK2 controls an EndoA phosphorylation cycle in synaptic endocytosis. Neuron *75*, 1008–1021.

Menzies, F.M., Fleming, A., and Rubinsztein, D.C. (2015). Compromised autophagy and neurodegenerative diseases. Nat. Rev. Neurosci. *16*, 345–357.

Milosevic, I., Giovedi, S., Lou, X., Raimondi, A., Collesi, C., Shen, H., Paradise, S., O'Toole, E., Ferguson, S., Cremona, O., and De Camilli, P. (2011). Recruitment of endophilin to clathrin-coated pit necks is required for efficient vesicle uncoating after fission. Neuron *72*, 587–601.

Nakamura, T., and Lipton, S.A. (2009). Cell death: protein misfolding and neurodegenerative diseases. Apoptosis *14*, 455–468.

Nixon, R.A. (2013). The role of autophagy in neurodegenerative disease. Nat. Med. *19*, 983–997.

Nonis, D., Schmidt, M.H., van de Loo, S., Eich, F., Dikic, I., Nowock, J., and Auburger, G. (2008). Ataxin-2 associates with the endocytosis complex and affects EGF receptor trafficking. Cell. Signal. *20*, 1725–1739.

Perera, R.M., Zoncu, R., Lucast, L., De Camilli, P., and Toomre, D. (2006). Two synaptojanin 1 isoforms are recruited to clathrin-coated pits at different stages. Proc. Natl. Acad. Sci. USA *103*, 19332–19337.

Petrelli, A., Gilestro, G.F., Lanzardo, S., Comoglio, P.M., Migone, N., and Giordano, S. (2002). The endophilin-CIN85-Cbl complex mediates ligand-dependent downregulation of c-Met. Nature *416*, 187–190.

Puri, C., Renna, M., Bento, C.F., Moreau, K., and Rubinsztein, D.C. (2014). ATG16L1 meets ATG9 in recycling endosomes: additional roles for the plasma membrane and endocytosis in autophagosome biogenesis. Autophagy *10*, 182–184.

Quadri, M., Fang, M., Picillo, M., Olgiati, S., Breedveld, G.J., Graafland, J., Wu, B., Xu, F., Erro, R., Amboni, M., et al.; International Parkinsonism Genetics Network (2013). Mutation in the SYNJ1 gene associated with autosomal recessive, early-onset Parkinsonism. Hum. Mutat. *34*, 1208–1215.

Raimundo, N., Song, L., Shutt, T.E., McKay, S.E., Cotney, J., Guan, M.X., Gilliland, T.C., Hohuan, D., Santos-Sacchi, J., and Shadel, G.S. (2012). Mitochondrial stress engages E2F1 apoptotic signaling to cause deafness. Cell *148*, 716–726.

Ralser, M., Nonhoff, U., Albrecht, M., Lengauer, T., Wanker, E.E., Lehrach, H., and Krobitsch, S. (2005). Ataxin-2 and huntingtin interact with endophilin-A complexes to function in plastin-associated pathways. Hum. Mol. Genet. *14*, 2893–2909.

Ravikumar, B., Moreau, K., Jahreiss, L., Puri, C., and Rubinsztein, D.C. (2010a). Plasma membrane contributes to the formation of pre-autophagosomal structures. Nat. Cell Biol. *12*, 747–757.

Ravikumar, B., Moreau, K., and Rubinsztein, D.C. (2010b). Plasma membrane helps autophagosomes grow. Autophagy *6*, 1184–1186.

Renard, H.-F., Garcia-Castillo, M.D., Chambon, V., Lamaze, C., and Johannes, L. (2015). Shiga toxin stimulates clathrin-independent endocytosis of the VAMP2, VAMP3 and VAMP8 SNARE proteins. J Cell Sci. *128*, 2891–2902.

Ringstad, N., Nemoto, Y., and De Camilli, P. (1997). The SH3p4/Sh3p8/SH3p13 protein family: binding partners for synaptojanin and dynamin via a Grb2-like Src homology 3 domain. Proc. Natl. Acad. Sci. USA *94*, 8569–8574.

Ringstad, N., Gad, H., Löw, P., Di Paolo, G., Brodin, L., Shupliakov, O., and De Camilli, P. (1999). Endophilin/SH3p4 is required for the transition from early to late stages in clathrin-mediated synaptic vesicle endocytosis. Neuron *24*, 143–154.

Ringstad, N., Nemoto, Y., and De Camilli, P. (2001). Differential expression of endophilin 1 and 2 dimers at central nervous system synapses. J. Biol. Chem. *276*, 40424–40430.

Saheki, Y., and De Camilli, P. (2012). Synaptic vesicle endocytosis. Cold Spring Harb. Perspect. Biol. *4*, a005645.

Sandri, M., Sandri, C., Gilbert, A., Skurk, C., Calabria, E., Picard, A., Walsh, K., Schiaffino, S., Lecker, S.H., and Goldberg, A.L. (2004). Foxo transcription factors induce the atrophy-related ubiquitin ligase atrogin-1 and cause skeletal muscle atrophy. Cell *117*, 399–412.

Schreij, A.M., Fon, E.A., and McPherson, P.S. (2016). Endocytic membrane trafficking and neurodegenerative disease. Cell. Mol. Life Sci. *73*, 1529–1545.

Shi, M., Bradner, J., Bammler, T.K., Eaton, D.L., Zhang, J., Ye, Z., Wilson, A.M., Montine, T.J., Pan, C., and Zhang, J. (2009). Identification of glutathione S-transferase pi as a protein involved in Parkinson disease progression. Am. J. Pathol. *175*, 54–65.

Soubeyran, P., Kowanetz, K., Szymkiewicz, I., Langdon, W.Y., and Dikic, I. (2002). Cbl-CIN85-endophilin complex mediates ligand-induced downregulation of EGF receptors. Nature *416*, 183–187.

Soukup, S., Kuenen, S., Vanhauwaert, R., Manetsberger, J., Hernández-Díaz, S., Swerts, J., Schoovaerts, N., Vilain, S., Gounko, N.V., Vints, K., et al. (2016). A LRRK2-dependent EndophilinA phosphoswitch is critical for macroautophagy at presynaptic terminals. Neuron *92*, Published online October 6, 2016. http://dx.doi.org/10.1016/j.neuron.2016.09.037.

Strohecker, A.M., Joshi, S., Possemato, R., Abraham, R.T., Sabatini, D.M., and White, E. (2015). Identification of 6-phosphofructo-2-kinase/fructose-2,6-bisphosphatase as a novel autophagy regulator by high content shRNA screening. Oncogene *34*, 5662–5676.

Takahashi, Y., Meyerkord, C.L., Hori, T., Runkle, K., Fox, T.E., Kester, M., Loughran, T.P., and Wang, H.G. (2011). Bif-1 regulates Atg9 trafficking by mediating the fission of Golgi membranes during autophagy. Autophagy *7*, 61–73.

Tong, Y., Giaime, E., Yamaguchi, H., Ichimura, T., Liu, Y., Si, H., Cai, H., Bonventre, J.V., and Shen, J. (2012). Loss of leucine-rich repeat kinase 2 causes age-dependent bi-phasic alterations of the autophagy pathway. Mol. Neurodegener. *7*, 2.

Trempe, J.F., Chen, C.X., Grenier, K., Camacho, E.M., Kozlov, G., McPherson, P.S., Gehring, K., and Fon, E.A. (2009). SH3 domains from a subset of BAR proteins define a Ubl-binding domain and implicate parkin in synaptic ubiquitination. Mol. Cell *36*, 1034–1047.

Verstreken, P., Kjaerulff, O., Lloyd, T.E., Atkinson, R., Zhou, Y., Meinertzhagen, I.A., and Bellen, H.J. (2002). Endophilin mutations block clathrin-mediated endocytosis but not neurotransmitter release. Cell *109*, 101–112.

Webb, A.E., and Brunet, A. (2014). FOXO transcription factors: key regulators of cellular quality control. Trends Biochem. Sci. *39*, 159–169.

Wong, A.S., Lee, R.H., Cheung, A.Y., Yeung, P.K., Chung, S.K., Cheung, Z.H., and Ip, N.Y. (2011). Cdk5-mediated phosphorylation of endophilin B1 is required for induced autophagy in models of Parkinson's disease. Nat. Cell Biol. *13*, 568–579.

Wu, C.L., Kandarian, S.C., and Jackman, R.W. (2011). Identification of genes that elicit disuse muscle atrophy via the transcription factors p50 and Bcl-3. PLoS ONE *6*, e16171.

Xie, P., Guo, S., Fan, Y., Zhang, H., Gu, D., and Li, H. (2009). Atrogin-1/MAFbx enhances simulated ischemia/reperfusion-induced apoptosis in cardiomyocytes through degradation of MAPK phosphatase-1 and sustained JNK activation. J. Biol. Chem. *284*, 5488–5496.

Xu, P., Das, M., Reilly, J., and Davis, R.J. (2011). JNK regulates FoxO-dependent autophagy in neurons. Genes Dev. *25*, 310–322.

Zaglia, T., Milan, G., Ruhs, A., Franzoso, M., Bertaggia, E., Pianca, N., Carpi, A., Carullo, P., Pesce, P., Sacerdoti, D., et al. (2014). Atrogin-1 deficiency promotes cardiomyopathy and premature death via impaired autophagy. J. Clin. Invest. *124*, 2410–2424.

Cell Reports, Volume *17*

Supplemental Information

Endophilin-A Deficiency Induces the Foxo3a-Fbxo32 Network in the Brain and Causes Dysregulation of Autophagy and the Ubiquitin-Proteasome System

John D. Murdoch, Christine M. Rostosky, Sindhuja Gowrisankaran, Amandeep S. Arora, Sandra-Fausia Soukup, Ramon Vidal, Vincenzo Capece, Siona Freytag, Andre Fischer, Patrik Verstreken, Stefan Bonn, Nuno Raimundo, and Ira Milosevic

Endophilin-A deficiency induces the FOXO3a-FBXO32 network in the brain and causes dysregulation of autophagy and the ubiquitin-proteasome system

John D. Murdoch[1,2]*, Christine M. Rostosky[1]*, Sindhuja Gowrisankaran[1], Amandeep S. Arora[1], Sandra F. Soukup[3,4], Ramon Vidal[5], Vincenzo Capece[5], Siona Freytag[1], Andre Fischer[6,7], Patrik Verstreken[3,4], Stefan Bonn[5], Nuno Raimundo[2]**, Ira Milosevic[1]**

Supplemental Figures and Figure legends

Figure S1, related to Figure 1

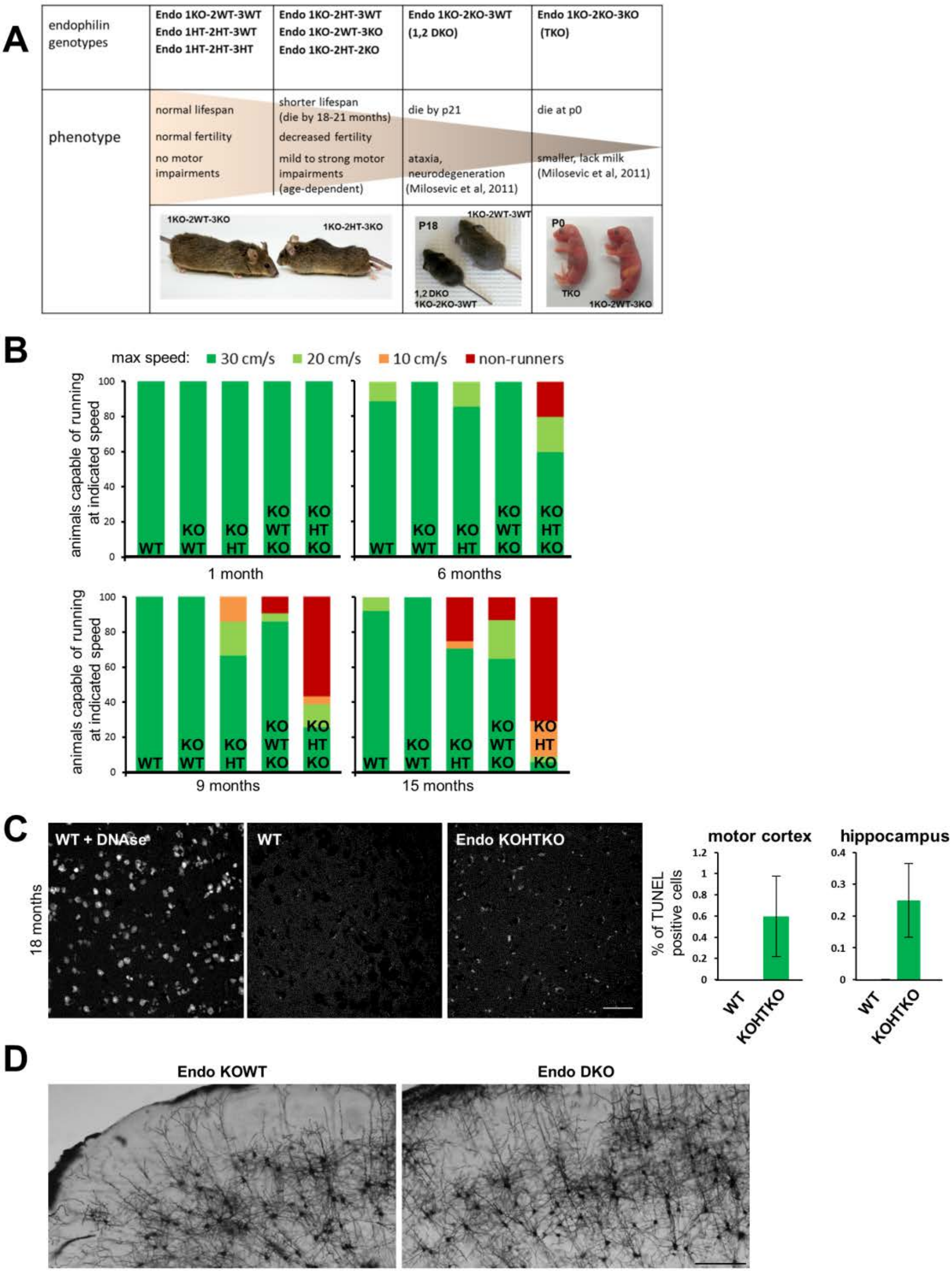

Figure S1. Motor impairments and neuronal cell death in mice with endophilin deficiency, related to Figure 1

(A) Schematic illustrating correlation between genotype and phenotype of endophilin mutant mice. Mammals have 3 endophilin-A genes (SH3GL2/endophilin-A1; SH3GL1/endophilin-A2; SH3GL3/endophilin-A3). Mice lacking endophilin-1 and 2 (1,2 DKO) and mice lacking all three endophilins (TKO) have impaired endocytosis and altered synaptic vesicle recycling. Endophilin TKO mice die 4-12 hours after birth, while endophilin 1,2 DKO live 2-3 weeks, show ataxia and mild to moderate neurodegeneration. Endophilin-1 single knock-out (KO) and heterozygous (1HT-2HT; 1HT-2HT-3HT) mice appear phenotypically normal and have normal lifespan, while endophilin 1KO-2HT and particularly 1KO-2HT-3KO mice exhibit shorter lifespans (~19 and ~18 months, respectively). Movie 1 and 2 show motor impairments in 1,2 DKO and 1KO-2HT-3KO mice that is independent from animal background (129Sv/J and 129Sv/J backcrossed to C56BL/6J).

(B) Highest speed that endophilin mutants were able to run on DigiGait at 1 (top-left), 6 (top-right), 9 (buttom-left) and 15 (buttom-right) months. Colors indicate percentage of mice able to run at 30 cm/s (green), 20 cm/s (light green), 10 cm/s (orange); red indicates animals refusing to run.

(C) Apoptosis in aged endophilin 1KO-2HT-3KO mice at 18 months: TUNEL assay was performed on brain sections of mice with indicated genotypes. DNAse treated WT sections were used as positive control for condensed DNA in the nucleus (shown by arrows) Scale bar 50µm. Right: Quantification of positive cells in motor cortex and hippocampus. Data are expressed as mean±SEM.

(D) Cortex of endophilin 1,2 DKO (p18) and littermate control by Golgi staining. Overall cell morphology is not altered. Scale bar: 200µm.

Figure S2, related to Figures 2 and 3

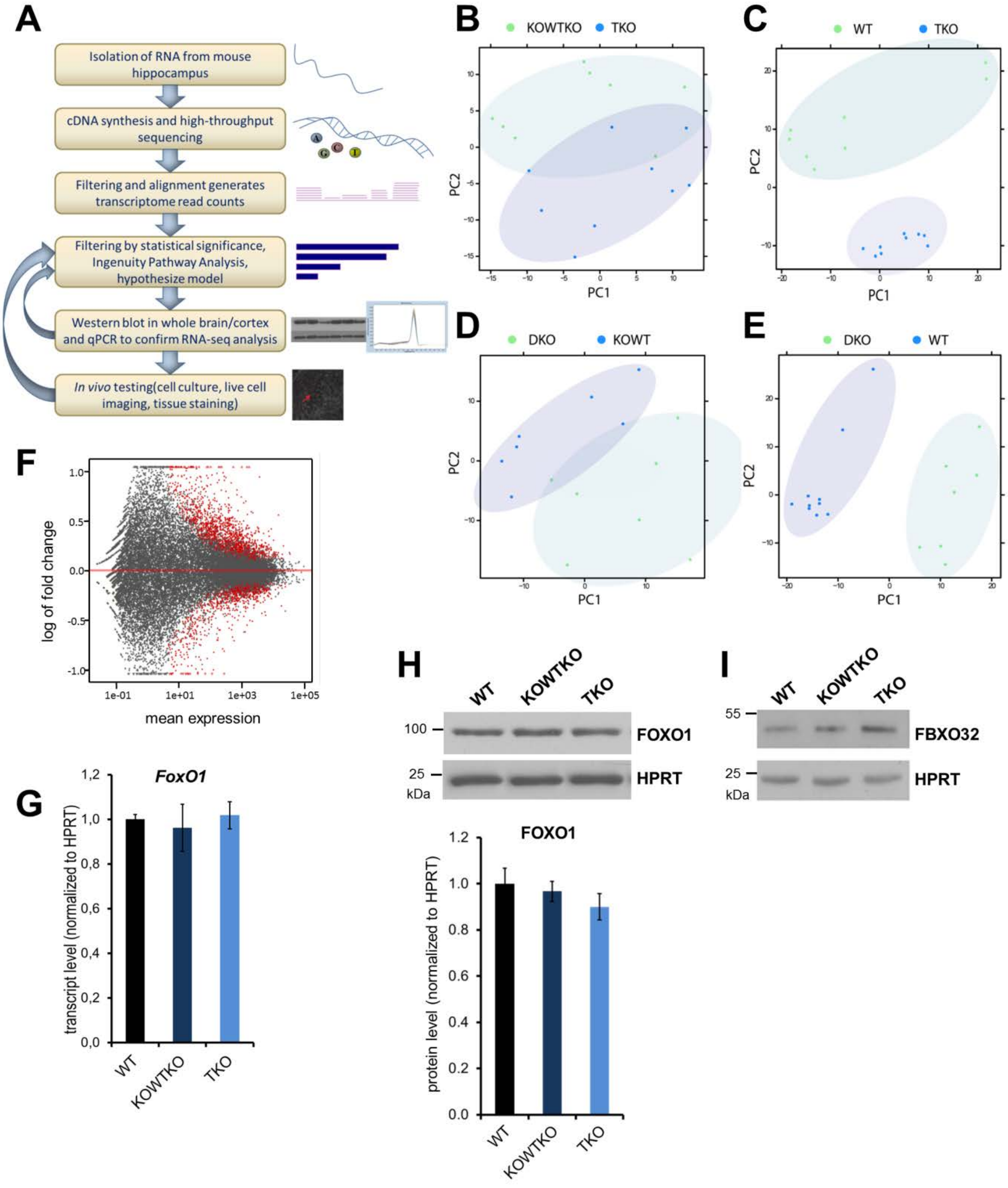

Figure S2. Integrative genomic analysis of endophilin TKO and 1,2 DKO hippocampi and verification experiments, related to Figures 2 and 3

(A) Experimental strategy highlighting the steps of RNA isolation from hippocampus, sequencing, mapping, statistical analysis and data verification.

(B) Endophilin TKO and littermate endophilin 1KO-2WT-3KO mice RNA-sequencing samples as assessed by principal component (PC) analysis. Data are present in Suppl Table 2.

(C) Endophilin TKO RNA-sequencing samples clearly segregated from WT samples by principal component analysis. Data are presented in Suppl Table 3.

(D) RNA-sequencing samples from endophilin 1,2 DKO and littermate endophilin 1KO-2WT mice as assessed by principal component analysis. Data are presented in Suppl Table 5.

(E) Endophilin 1,2 DKO RNA-sequencing samples clearly segregated from WT samples by principal component analysis. Data are presented in Suppl Table 6.

(F) RNA-sequencing of endophilin TKO vs. control (WT+littermates) hippocampi samples yield 2176 differentially expressed genes with nominal p-value<0.01. Data are presented in Suppl Table 7 and shown here in a volcano plot depicting the logarithmic fold change and the mean expression. Each dot represents one gene; the differentially expressed genes are depicted in red.

(G) Transcript levels of *Foxo1*, as measured by quantitative real-time PCR, in endophilin TKO samples and corresponding controls. p>0.05, Student’s t test, error bars: SEM.

(H) Protein analysis by Western blotting revealed no change in FOXO1 levels in endophilin TKO whole brain extracts in comparison to corresponding controls. Below: Quantification of immunoblots for FOXO1 (normalized to the loading control). p>0.05, Student’s t test, error bars: SEM.

(I) Representative Western blot showing upregulation of FBXO32 in endophilin TKO hippocampus (compared to WT and littermate control). The loading control (HPRT) is shown below.

Figure S3, related to Figures 3 and 4

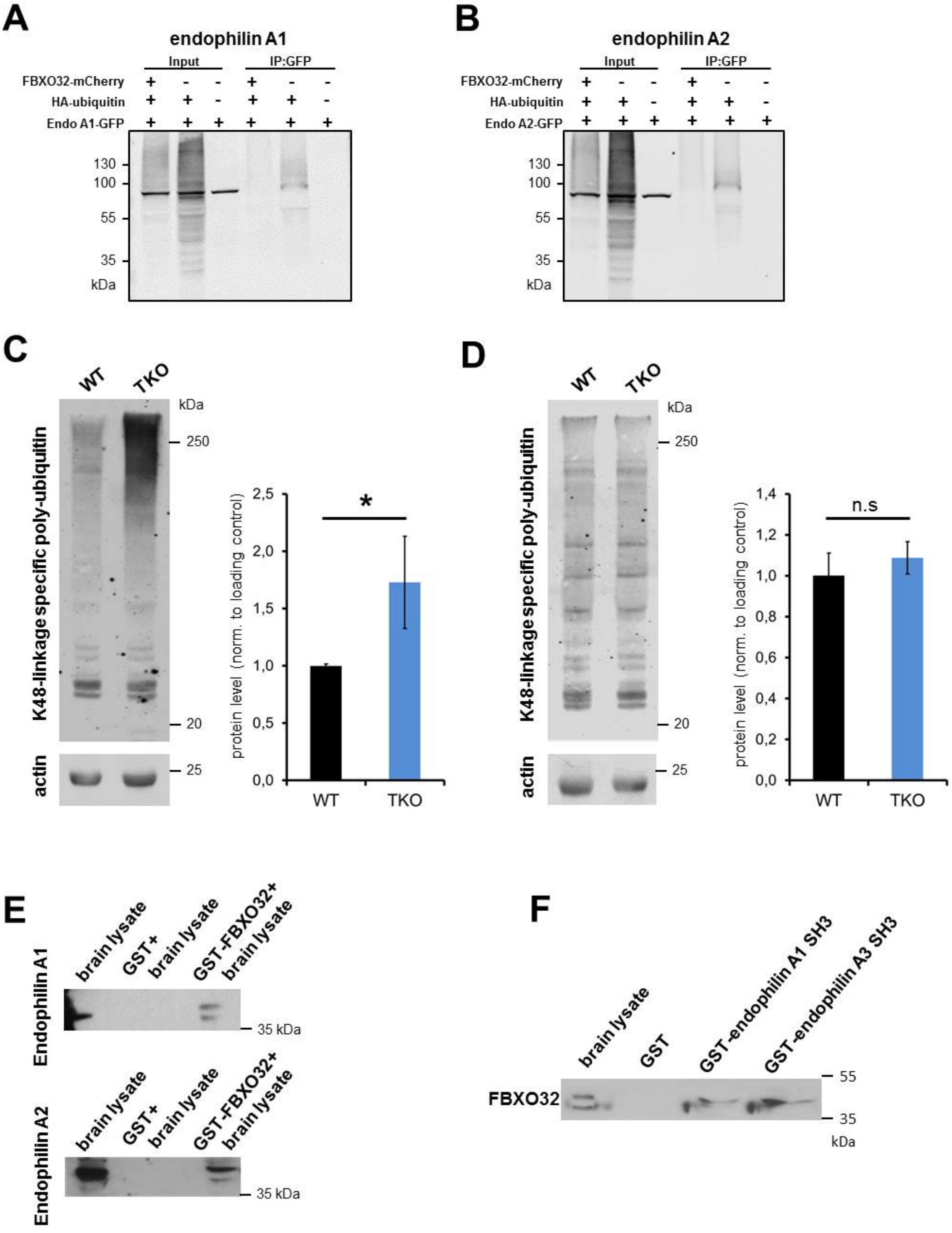

Figure S3. **FBXO32 does not ubiquitinate endophilin-1 and 2, related to Figures 3 and 4**

(A) FBXO32 does not ubiquitinate endophilin-1. Analysis of *in vivo* ubiquitination: EGFP-endophilin-1 was co-expressed with HA-ubiquitin in the presence or absence of FBXO32-mCherry. HeLa cell extracts were subjected to immunoprecipitation with anti-GFP antibody and protein ubiquitination was detected by anti-HA Western blotting. Experiment was repeated 3 times (the same result was obtained each time).

(B) FBXO32 does not ubiquitinate endophilin-2. Analysis of *in vivo* ubiquitination: EGFP-endophilin-2 was co-expressed with HA-ubiquitin in the presence or absence of co-expressed FBXO32-mCherry. HeLa cell extracts were subjected to immunoprecipitation with anti-GFP antibody and protein ubiquitination was detected by anti-HA Western blotting. Experiment was repeated 2 times (the same result was obtained each time).

(C) Overall increase in K48-linked (proteasome targeting) ubiquitination in endophilin TKO brains, determined by Western blotting. Right: Quantification from 5 samples/genotype. *$p<0.01$, Student's t test, error bars: SEM.

(D) No change in K63-linked (proteasome-unrelated) ubiquitination in endophilin TKO brains, as determined by Western blotting. Right: Quantification from 5 samples/genotype. $p>0.05$, Student's t test, error bars: SEM.

(E) Endophilin-3 interacts with FBXO32. Representative Western blots from 3 independent experiments of anti-GFP immunoprecipitation from HeLa cell lysate probed with anti-RFP antibody.

(F) GST pull-down from mouse brain lysates using the SH3 domains of endophilin 1, 2 and 3 as baits. Note FBXO32 stronger binding to endophilin-1 and 3 SH3's domains (when films were overexposed, weak band in endophilin-2 SH3 domain sample could also be detected). The experiment was repeated twice.

Figure S4, related to Figure 5

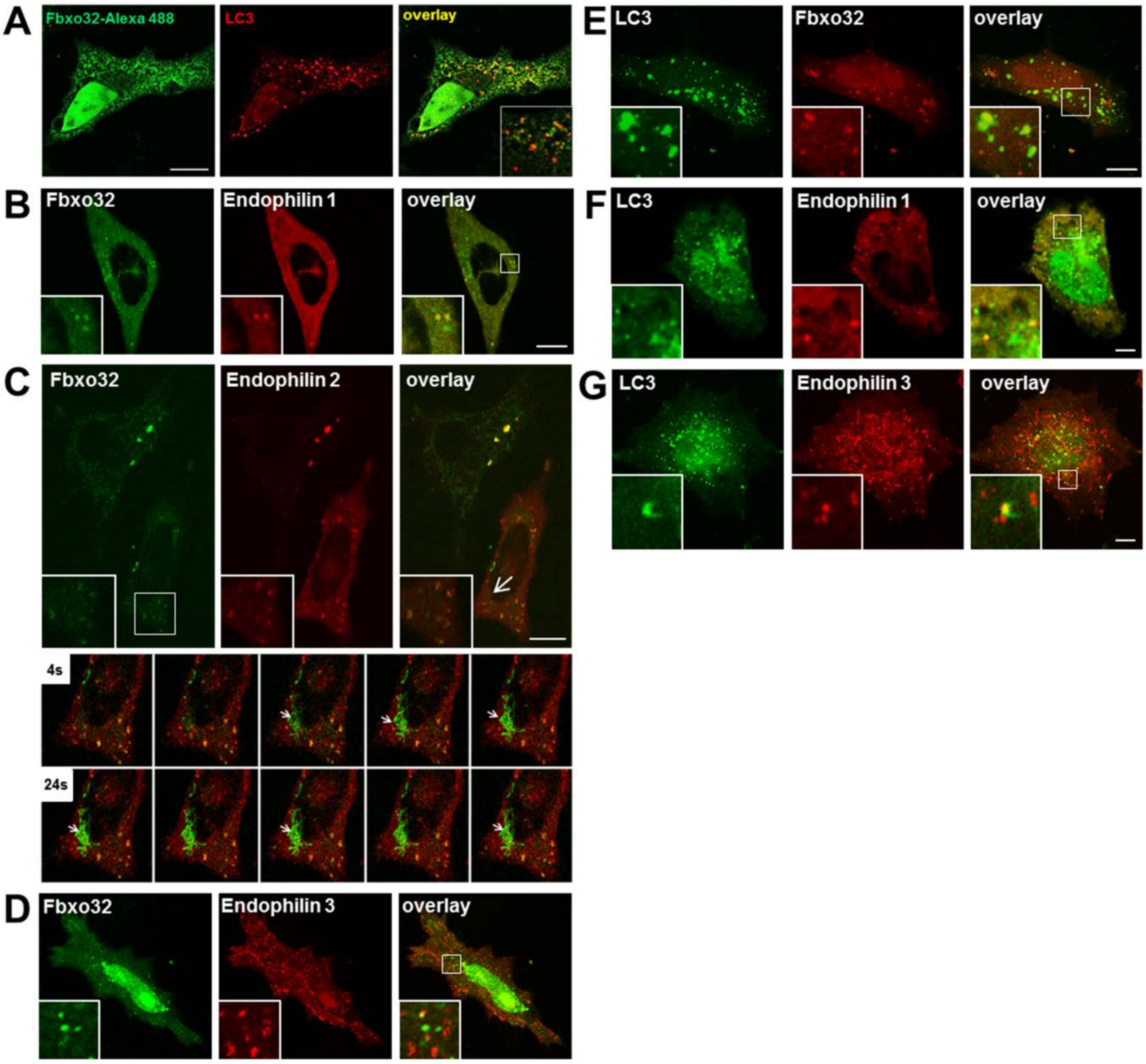

Figure S4. FBXO32 tubulates membranes and co-localizes with clathrin-coated structures and LC3-labelled autophagosomes, related to Figure 5

(A) Native FBXO32 distribution (as detected by immunostaining against FBXO32) in cultured HeLa cell is similar to distribution of overexpressed FBXO32: FBXO32 immunofluorescence was detected in the nucleus and cytosol, and it co-localized partially with autophagosomal maker LC3 (magnified in the inset). Scale bar: 5 µm.

(B) FBXO32-EGFP colocalizes transiently with endophilin-1-mRFP. HeLa cell expressing FBXO32-EGFP (left) and endophilin-1-mRFP (middle); magnified in the inset. Note FBXO32’s distribution in the presence of endophilin-1: FBXO32 is mainly extra-nuclear and cytosolic. Scale bar 5 µm.

(C) FBXO32-EGFP colocalizes partially with endophilin-2-RFP (magnified in the inset). A representative MEF with overexpressed FBXO32-EGFP (left) and endophilin-2-mRFP (middle) imaged by spinning-disk confocal microscopy. Scale bar: 5 µm. Below: Image gallery from live time-lapse spinning-disk microscopy from the area indicated by arrow depicting potent tubulation and recruitment of FBXO32 to the tubulating membranes.

(D) FBXO32-mCherry colocalizes transiently with endophilin-3-EGFP. HeLa expressing FBXO32 (left) and endophilin-3 (middle); magnified in the inset. Same magnification is in (A). Images (A-D) were acquired by spinning-disk microscopy.

(E) HeLa cell expressing LC3-EGFP (left) and FBXO32-mCherry (middle) for 26h; starved for 2-3h. Scale bar 5 µm.

(F) Endophilin-A1 showed sparse colocalization with LC3, implying a transient association of endophilin-A1 with autophagosomes. HeLa cells expressing LC3-EGFP (left) and endophilin-A1 protein (middle) were imaged by spinning-disk confocal microscopy after being starved for 2-3h; image on the right shows the overlay. Scale bar 3 µm.

(G) Endophilin-A2 showed sparse colocalization with LC3, implying a transient association of endophilin-A1 with autophagosomes. HeLa cells expressing LC3-EGFP (left) and endophilin-A2 protein (middle) were imaged by spinning-disk confocal microscopy after being starved for 2-3h; image on the right shows the overlay. Scale bar 3 µm.

Figure S5, related to Figure 6

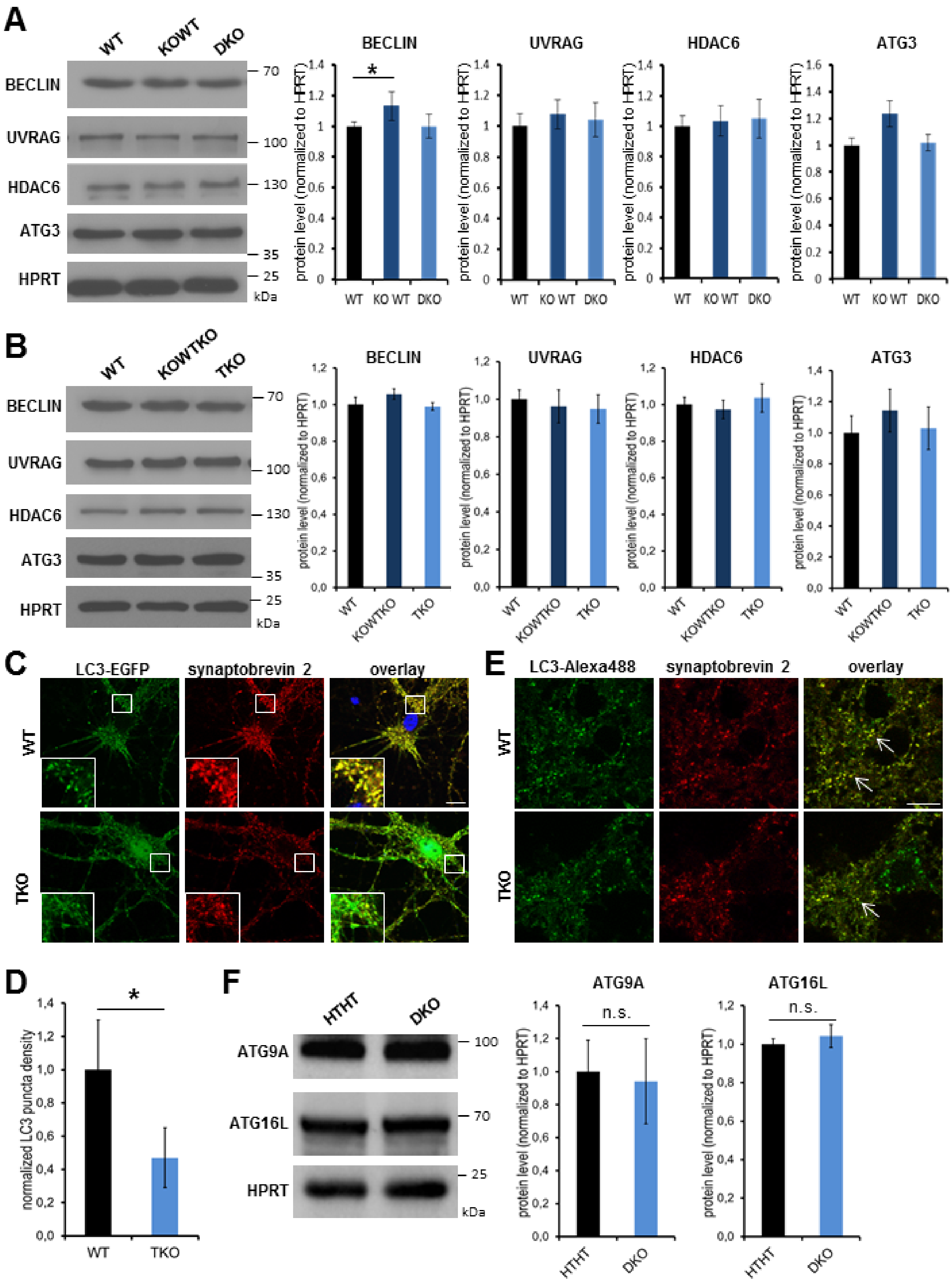

Figure S5. No change in proteins necessary for autophagosome formation or signaling that represses autophagosome formation in endophilin TKO and 1,2 brains, related to Figure 6

(A) Protein analysis by Western blotting revealed no changes in the levels of autophagosomal proteins BECLIN, UVRAG, HDAC6 and ATG3 in endophilin DKO cortex. Right: Histograms showing quantification of the immunoblotting, normalized to the loading control HPRT (at least 6 samples/genotype). p>0.05, Student's t test, error bars: SEM.

(B) Protein analysis by Western blotting revealed no changes in the levels of autophagosomal proteins BECLIN, UVRAG, HDAC6 and ATG3 in endophilin TKO whole brain extracts. Right: Histograms showing quantification of the immunoblotting, normalized to the loading control HPRT (at least 8 samples/genotype). p>0.05, Student's t test, error bars: SEM.

(C) Autophagosomal marker LC3 revealed less prominent accumulation of LC3 at the synapses of primary endophilin TKO hippocampal neurons. Neurons were treated with 250 nM Torin-1 for 4 hours in the EBSS buffer to accumulate autophagosomes. Note that LC3-signal in WT neuronal processes is a bit more punctate than in TKO neuronal processes, and that WT neurons show better overlap (yellowish signal in the WT overlay, greenish in the TKO overlay) between LC3 and synaptic maker synaptobrevin-2. Scale bar: 5μm.

(D) Decreased LC3 (autophagosome) signal in the endophilin TKO hippocampal cultures: y-axis represents the density of LC3 fluorescence puncta normalized to controls. Three independent experiments were performed and at least 16 images per condition were analyzed. *p<0.05, Student's t test; error bars: SEM.

(E) Immunostaining for LC3 (autophagosomal marker) and synaptobrevin-2 (synaptic marker) in primary neurons prepared from WT and endophilin TKO hippocampi. Neurons were treated as described above. There is less prominent accumulation of LC3-signal at the synapses in endophilin TKO neurons. LC3-positive autophasomal structures in the cell body (blue arrow) seem less affected than LC3-positive autophagosomal structures at the synapses (white arrow) in endophilin TKO neurons. Scale bar: 5μm.

(F) Protein analysis by Western blotting revealed no changes in the levels of autophagosomal proteins ATG9A and ATG16L in endophilin 1,2 DKO cortexes. Right: Histograms showing quantification of the immunoblotting, normalized to the loading control HPRT (at least 4 samples/genotype). p>0.05, Student's t test, error bars: SEM.

Figure S6, related to Figure 7

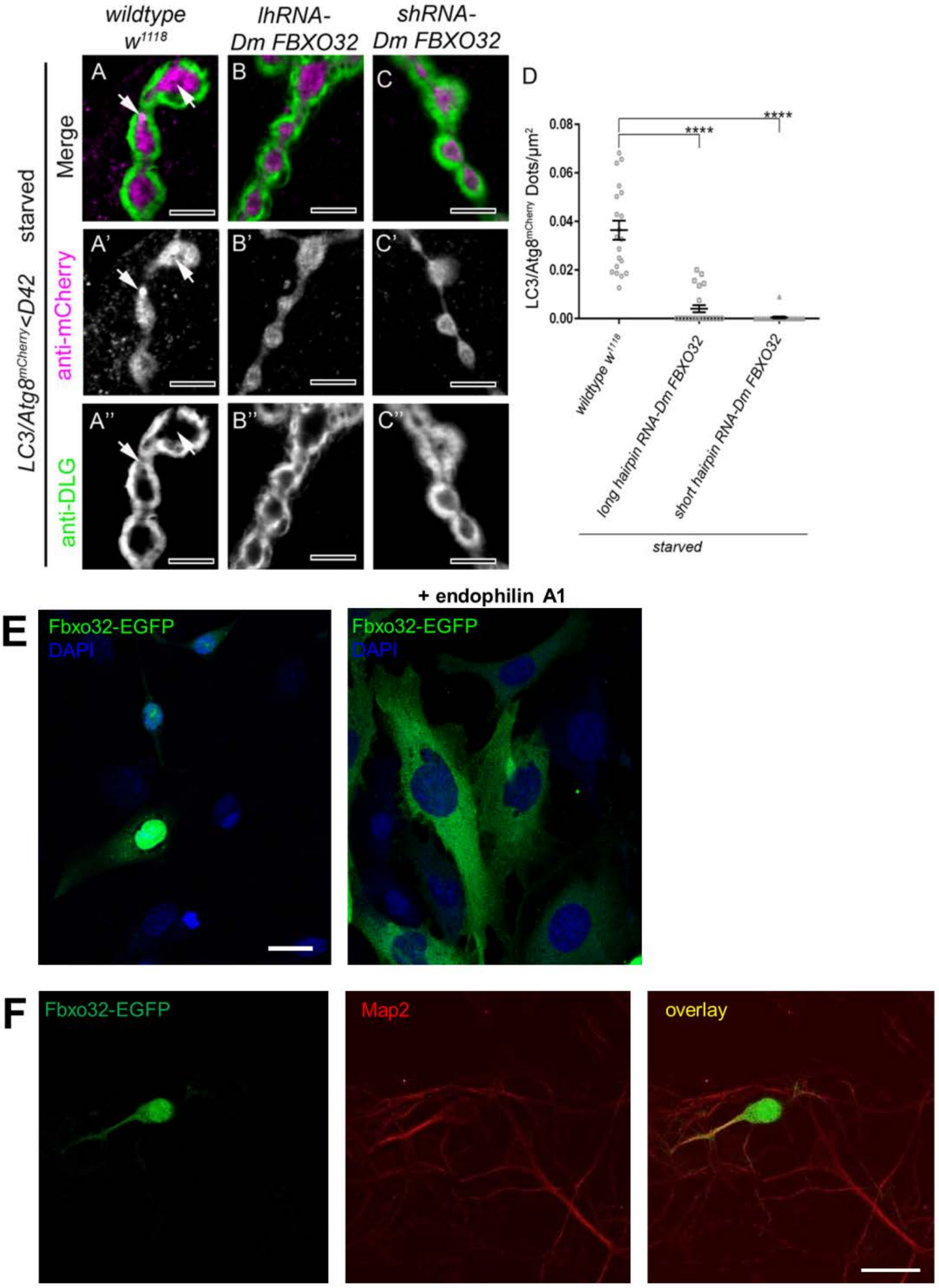

Figure S6. FBXO32 is required for autophagy at drosophila NMJ and its upregulation causes apoptosis in cultured primary neuronal cells, related to Figure 7.

(A-C'') Confocal imaging of 4 h-starved neuromuscular junction boutons (NMJ) of WT control animals (A-A''), animals expressing long hairpin RNAi against Drosophila FBXO32 (B-B'') and animals expressing short hairpin RNAi against Drosophila FBXO32 (C-C'') co-expressing ATG8-mCherry under control of the D42-Gal4 driver to drive expression in the motor neurons and NMJ. (A-C) Shows merged images of anti-mCherry (magenta, A'-C') to mark autophagosomes (arrows in A-A') and anti-DLG (green, A''-C'') to label the post synaptic site.

(D) Quantification of the number of ATG8-mCherry dots per bouton area (arrows) and statistical analysis using 1-way ANOVA followed by Post Hoc Mann-Whitney test ****$p<0.0001$, $n>21$. Individual data points are shown and the mean±SD is indicated. Scale bars: 5 µm

(E) Representative images of fixed HeLa cells co-transfected with FBXO32-EGFP and mRFP (left) and FBXO32-EGFP and endophilin-1-mRFP (right) for 30h, co-stained with DAPI. mRFP and endophilin-1-mRFP signals are not shown to emphasize the difference in FBXO32 distribution. Gain was kept constant for all images. Note that less than 50% of FBXO32-transfected cells survive on average (left image). Scale bar: 7 µm.

(F) Primary hippocampal neurons transfected with FBXO32-EGFP under chicken-β-actin promoter. Neurons were transfected on DIV0 by electroporation, fixed on DIV14, co-stained for MAP2 and imaged by confocal microscopy. Less than 15% FBXO32-transfected neurons are detected at DIV14 (when compared to EGFP-expressing neurons). The surviving FBXO32-transfected neurons did not appear healthy and had only few short processes. Scale bar: 7 µm.

Supplemental Movies

Movie S1. Endophilin 1,2 DKO and littermate 1KO-2WT mice, related to Figure 1. Mice have a 129Sv/J background (all our endophilin lines, including 1,2 DKO, were also backcrossed to C56BL/6J for 5 generations). Endophilin 1,2 DKO mouse displays ataxia (staggering, lack of balance, loss of muscle control, slow eye movement, etc.), littermate 1KO-2WT mouse does not have obvious movement deficits.

Movie S2. Endophilin 1KO-2WT-3KO and endophilin 1KO-2HT-3KO mice running in a DigiGait treadmill at 20 cm/s, related to Figure 1. Left: endophilin 1KO-2WT-3KO, right endophilin 1KO-2HT-3KO. Top: video, bottom: extracted paw signal by DigiGait analysis software. Note that endophilin 1KO-2HT-3KO mice have an altered walking pattern (real-time video rate has been slowed down 3x).

Movie S3. FBXO32-EGFP expressed in MEF for 22h and imaged by spinning-disc confocal microscopy, related to Figure 5. This movie shows distribution of FBXO32 in MEF: FBXO32 is predominantly cytosolic, although it often accumulated in the nucleus; it is enriched at dynamic organelle-like structures exemplifying its role in trafficking. Time-lapse images were captured every 4s, video runs at 10 frames/s.

Movie S4. FBXO32-EGFP and LC3-mRFP expressed in HeLa for 28h and imaged by spinning-disc confocal microscopy, related to Figure 5. The movie shows FBXO32 (green) association with LC3-positive autophagosomes (red). Time-lapse images were captured every 4s, video runs at 10 frames/s.

Movie S5. FBXO32-EGFP and endophilin-2-mRFP expressed in MEF for 21h, related to Figure 5. Imaged by spinning-disc confocal microscopy. Note that FBXO32 (green) and endophilin (red) co-localized on trafficking organelles and tubular structures. **Inset** shows a zoomed image with dynamic tubule labelled with both FBXO32-EGFP and endophilin-2-mRFP. Time-lapse images were captured every 4s, video runs at 10 frames/s.

Movie S6. Magnified view of HeLa expressing FBXO32-EGFP (green), LC3-mRFP (red) and endophilin-2-iRFP (magenta) for 22h, related to Figure 5. Imaged by spinning-disc confocal microscopy. Size of inset 3 µm. Time-lapse images were captured every 4s, video runs at 10 frames/s

Movie S7. Magnified view of hippocampal neuron expressing endophilin-2-EGFP (green) and ATG5-mCherry (red), related to Figure 5. Imaged by spinning-disc confocal microscopy. Size of inset 4 µm. Time-lapse images were captured every 4s, video runs at 10 frames/s.

Tables

Table 1-7: See attached Excel file

Table 1. RNA sequencing of endophilin TKO and endophilin 1,2 DKO samples, related to Figure 2. Genotype, total reads and mapped reads are shown for each sample.

Table 2. Comparison of endophilin TKO and littermate 1KO-2WT-3KO samples, related to Figure 2. The ENSEMBL gene identifier is the key identifier for each gene. Shown for each gene, from left to right, are the corresponding gene symbol, description, genomic coordinates (including chromosome, with start and end positions), average reads across all samples, average reads across KOWTKO samples, average reads across TKO samples, logarithm (base 2) of the fold change between the average TKO reads and the average KOWTKO reads, nominal p-value and adjusted p-value.

Table 3. Comparison of endophilin TKO and WT samples, related to Figure 2. The ENSEMBL gene identifier is the key identifier for each gene. Shown, from left to right are the corresponding gene name, description, genomic coordinates (including chromosome, with start and end positions), average reads across all samples, average reads across WT samples, average reads across TKO samples, logarithm (base 2) of the fold change between the average TKO reads and the average WT reads, nominal p-value and adjusted p-value.

Table 4. Crossing of TKO and 1,2 DKO differentially-expressed genes with gene lists of ataxia and Parkinson's disease, related to Figure 2. For each comparison between endophilin mutants and controls (1,2DKOxWT, 1,2DKOx1KO-2WT, TKOxWT, TKOx1KO-2WT-3KO), the threshold for differential expression was an adjusted p-value<0.01 and a $\log_2$FC>0.4. The genes that met those criteria were considered differentially-expressed genes (DEGs) for each comparison, and the number of genes is shown in the second column next to each comparison. The number of DEGs in each comparison that is also included in the ataxia and Parkinson's disease (PD) lists, the corresponding enrichment score and p-value are shown. The last columns indicate the symbols of the genes that are present in the DEG lists and also ataxia and PD for each comparison.

Table 5. Comparison of endophilin 1,2 DKO and 1KO-2WT samples, related to Figure 2. The ENSEMBL gene identifier is the key identifier for each gene. Also shown, from left to right are the corresponding gene name, description, genomic coordinates (including chromosome, with start and end positions), average reads across all samples, average reads across 1KO-2WT samples, average reads across 1,2 DKO samples, logarithm (base 2) of the fold change between the average 1,2 DKO reads and the average 1KO-2WT reads, nominal p-value and adjusted p-value.

Table 6. Comparison of endophilin 1,2 DKO and WT samples, related to Figure 2. The ENSEMBL gene identifier is the key identifier for each gene. Shown, from left to right are the corresponding gene name, description, genomic coordinates (including chromosome, with start and end positions), average reads across all samples, average reads across WT samples, average reads across 1,2 DKO samples, logarithm (base 2) of the fold change between the average 1,2 DKO reads and the average WT reads, nominal p-value and adjusted p-value.

Table 7. List of DEGs when endophilin TKO samples are compared against all controls pooled together, related to Figure 2. The threshold for differential expression was set at nominal p-value<0.01 to generate a gene list with optimal size for the pathway analysis algorithm (IPA software). For each gene, the ENSEMBL identifier and the fold change are presented.

Table 8. Upstream regulators of TKO transcriptome, related to Figure 2. These regulators were identified by Ingenuity Pathway Analysis, under the criteria of a p-value<0,05. To limit false positives, the analysis was restricted to the regulators that were present in the list of differentially expressed genes. The logarithm of the fold change for each regulator in the TKO dataset is presented.

Supplemental Experimental Procedures

Cell morphology assessment

Golgi staining was performed with the FD Rapid GolgiStain^{TM} Kit (FD Neurotechnologies Inc.) following the manufacturer's instructions. In short, animals were euthanized and the whole brain dissected, rinsed and immersed in the impregnation solution for 14 days. After 3 days incubation in solution C, brains were quickly frozen in isopentene using liquid nitrogen. Immediately after freezing, the brains were cut using a cryostat (Leica CM1859 UV) at 100 or 150 µm thickness and stained the next day. For staining, slides were incubated in working solution for 10 min and dehydrated before being embedded in Permount® (Entellan New, Merck). Samples were imaged on a Nikon AZ100 microscope.

RNA-sequencing

RNA for RNA-sequencing experiments was isolated using Tri-Reagent (Sigma) according to the manufacturer's instructions. RNA-seq libraries were prepared using the TruSeq® RNA Sample Preparation v2 kit and the TruSeq® Small RNA Preparation kit from Illumina. The library quality was checked using an Agilent 2100 Bioanalyzer and a Qubit dsDNA HS Assay Kit. The sample concentration was measured using a Qubit dsDNA HS Assay Kit and adjusted to 2 nM before sequencing (50 bp single end) on a HiSeq 2000 (Illumina) using TruSeq SR Cluster Kit v3-cBot-HS and TruSeq SBS Kit v3-HS according to the manufacturer's instructions. At least 7 biological replicates per condition were used for sequencing.

Read alignment and quality assessment: Murine RNA-seq data was aligned to the *Mus musculus* mm10 genome using STAR aligner (Version 2.3.0e_r291) with default options and generating alignment files in BAM format (Dobin et al., 2013). Read counts for all genes and all exons (Ensembl annotation v72) were obtained using FeaturesCount (version 1.4.6) (Liao et al., 2014). RNA-seq data was subjected to an in-house quality control workflow (Capece et al., 2015; Halder et al., 2016). During the quality assessment sequencing data was analyzed for the percentage of aligned, uniquely aligned and unaligned reads to determine possible sequencing biases, while sequencing depth was determined by the average per base coverage for each sample (Suppl. Table 1). Principal component analysis (PCA) was performed on RNA-seq expression values as previously described (Capece et al., 2015). One sample that did not meet quality standards was removed from further analysis.

Differential expression and pathway analysis: Read counts, as generated in the 'Read alignment and quality assessment' section, were used to find differentially expressed genes (DEGs) between the aforementioned mutant and control samples using DESeq2 (Love et al., 2014). Genes with an adjusted p-value smaller than 0.01 and an absolute $\log_2$ fold change (logFC) higher than 0.4 were considered to be DEGs. Results of the differential expression analysis can be found in Supp Table 1-3 and 5-6. For functional enrichment analyses we used Webgestalt and only considered categories significant with an adjusted p-value < 0.05. Genes with a nominal p-value smaller than p=0.01 were considered to be DEGs for input into Ingenuity Pathways Analysis (IPA). In multiple instances, perturbation of the genomic surroundings of knocked-out genes have been reported (Chandrasekharan et al, 2010; Rampon et al, 2008; Yang et al, 2007; Wang et al, 2014). After mapping the sequence reads to the transcriptome, we blocked the regions within 1 million base pairs of the genes knocked-out (endophilins 1, 2, 3), to ensure that genes whose expression may be affected by the perturbation of promoters or enhancers nearby are not skewing the pathway analysis.

Quantitative RT-PCR

RNA extraction and purification were performed using via Qiagen or Macherey-Nagel RNA extraction kits according to manufacturer's instructions. RNA quantification and quality control were done using Nanodrop (PeqLab), and cDNA was synthesized with High-Capacity cDNA Reverse Transcription Kit (Applied Biosystems) according to the manufacturer's instructions. cDNA was diluted 1:100, and each 8 µl reaction contained 4 µl diluted cDNA, 0,2 µl dilutions of each primer (from 25 µM stock) and 3,6 µl iTaq Universal SYBR Green Supermix (Bio-Rad).

Biochemical procedures

Brains or dissected brain samples were stored at -80°C long-term, and shortly before use were placed in -20°C blocks until being quickly added to tubes containing three 5mm metallic beads and 1080 µL of homogenization buffer [20mM HEPES pH 7.4, 150mM NaCl, 1mM EDTA, 1mM DTT, Complete Protease Inhibitor (Roche) and phosSTOP phosphatase inhibitor (Roche)] immediately prior to tissue homogenation. Samples were oscillated vigorously on the bead mill apparatus (Retsch MM400) for 1 minute at 20 Hz (p0 animals) or 30 Hz (1,2 DKO p14-21 and old animals). Samples were subjected to a 10s quick-spin and 120 µL of 20% sodium dodecyl sulfate (SDS) was added to completely solvate the high proportion of lipids and cholesterol in brain tissue. Samples were again subjected to 1 minute oscillation on the bead mill at 20 Hz for p0, and 30 Hz for young and old animals. A quick-spin again reduced the foam and bubbles. If any visible opaque streaks or solid matter remained at this point, the above two steps were repeated 1-2x. 18-20 month-old animals required 5 minutes of total homogenization and addition of greater volume to solvate the tissue – 2 additional 1-minute homogenizations after the 4th 1 minute homogenization step, an additional 300 uL of pre-mixed SDS and homogenization buffer (30 µL 20% SDS and 270 µL homogenization buffer) were added to solvate the remaining clumps of lipid and tissue. This volume was sufficient to homogenize the remaining solid matter for a final volume of 1500 µL in the old animals. The final homogenate was then subjected to vigorous mixing (15–30x) with a 27-gauge needle and 1 mL syringe to break up any semisolid remnants and shear viscous DNA strands so that the mixture was fluid and homogeneous for use in SDS-PAGE gels.

Samples were then quantitated with Pierce BCA (Thermo Scientific) in a 40x dilution to fall in the linear range as determined by the BSA standard curve using the BSA aliquot provided in the BCA kit. 3 µL of sample were diluted in 117 µL of dH_2O to give 120 µL of diluted sample, then 50 µL of diluted sample was added to 1 mL of the 1:50 BCA working solution. This last step was done in duplicate for each sample. These mixes were prepared in glass test tubes and incubated in a 37°C water bath for 30 minutes, then transferred to plastic cuvettes and read on a spectrophotometer (Eppendorf).

The SDS-PAGE gels were prepared at 1 mm thickness in 4% stacking and 12% resolving concentrations. For every multiple of 4 gels, the stacking component was prepared with 6.43 mL dH_2O, 2.5 mL 0.5M Tris-HCl pH 6.7, 100 µL 10% SDS, 1 mL 40% acrylamide-bis-acrylamide 30:1, 100 µL ammonium persulfate and 20 µL TEMED, and the resolving component was prepared with 8.7 mL dH_2O, 5 mL 1.5M Tris-HCl pH 8.7, 200 uL 10% SDS, 6 mL 40% acrylamide-bis-acrylamide 30:1, 200 uL ammonium persulfate and 20 uL TEMED. Gels were loaded with 50 ug of protein per well in volumes of 20 µL of diluted sample and 4 µL of 6x loading buffer (10 mL: 1.2 g sodium dodecyl sulfate, 4.7 mL glycerol, 1.2 mL 0.5M Tris pH 6.8, 0.93 g dithiothreitol, 6 mg bromophenol blue, 2.1 mL dH_2O). Samples were always diluted to a final concentration of 50 µg using additional sample buffer. Wells with no sample were filled with the corresponding buffer and loading buffer in the same proportion as for sample-containing wells (20 µL sample/buffer plus 4 µL loading buffer per well). Protein ladder was PageRuler Prestained Plus (Thermo Scientific).

Immunoprecipitation experiments: For Trap®-GFP immunoprecipitation, Hela cells ($1.2x10^6$) were plated in a 10cm plate and transfected with Lipofectamine 3000 after 3-4 hours. Endophilin-1, 2 or 3 tagged with EGFP were co-expressed either with FBXO32-mCherry or mCherry control (6.5µg/plate in total). The cells were harvested 30 hours after transfection and lysed. We used Chromotek Trap®-GFP agarose beads (Chromotek, Germany) and followed manufacturer’s protocol. The eluate was loaded onto SDS-PAGE gel followed by an immunoblot analysis for Cherry (RFP antibody 5F8, Chromtek, Germany) using standard protocol. Three independent experiments were performed.

Pull-down experiments: Pull-down experiments with GST-endophilin-1-SH3, GST-endophilin-2-SH3and GST-endophilin-3-SH3 domains were performed as previously described (Cao et al, 2014). The same method was used for GST-FBXO32 pull-down experiments. Three independent experiments were performed.

Autophagy in primary neurons and clonal cells

For autophagy-related experiments, we electroporated dissociated neurons in suspension (P3 Primary Cell 4D-Nucleofector® X Kit L, Amaxa, Lonza) before plating. If electroporation is used, it is essential that promoter is mild - all constructs used in neurons had chicken β-actin or synapsin promoter. For primary neuronal cell transfection, we followed manufacturer’s instructions (Lonza). On average, transfection efficiency of ~60% and ~70% neuronal survival was achieved (protocol CA138 and CL133, Nucleofactor-II). We used transfected neurons 12-16 days after transfection/plating (only strong, good-looking neuronal preparations where cell bodies and large processes were “shiny” and no cell inclusions/vacuoles or distressed cells were visible). Further, the osmolarity of neuronal medium was measured before experiment: osmolarity of buffers/solutions that were subsequently used was adjusted to match medium in which neurons grew. Buffers/solutions were warmed up to 37°C before use, and incubation with drugs was done in the incubator (37°C, 5% CO_2 in a humidified atmosphere). We used 250nM Torin-1 (BioVision) in the EBSS buffer (Gibco) without B27 supplement (Gibco) for 4 h to induce autophagy. Neurons were subsequently imaged by spinning-disk microscopy (Perkin Elmer Ultraview spinning-disk setup that consists of Nikon Ti-E Eclipse inverted microscope equipped with Perfect Focus, 60x CFI Plan Apo VC Nikon objective and 14 bit electron-multiplied CCD camera/Hamamatsu C9100), or fixed with 3,7% paraformaldehyde and 1% sucrose in the Tyrode buffer for 1h, immunostained for synaptic markers (e.g. synaptobrevin-2) and imaged by confocal microscopy (a LSM 710 setup by Zeiss). In neurons without autophagy induction, mildly expressed LC3 looked cytosolic with some brighter puncta. Upon autophagy induction, bright puncta were increased in cell periphery (processes) as well as in the cell body.

Endophilin TKO neurons have less synaptobrevin-2 (Milosevic *et al*., 2011), even so, the overlap between LC3 and synaptobrevin-2 was less prominent in endophilin TKO neurons.

Clonal cells (MEF, Hela) that mildly express fluorescently labelled-LC3 in addition to other probes (e.g. FBXO32, endophilins) were starved for at least 2 hours before being imaged by spinning-disk microscopy (the same setup as detailed above was used).

Colocalization analysis

Given that the majority of respective fluorescent signals were cytosolic, colocalization was evaluated semi-automatically using object-based overlap analysis and ImageJ JACoP plugin (Bolte and Cordelieres, 2006). In short, the image was first segmented into objects and background (i.e. bright fluorescent objects are segmented from the image) and then their spatial relationship (overlap) was measured. The same analysis was performed with flipped images and random colocalization was subtracted for every image.

The results were verified by complementary manual colocalization analysis based on morphological criteria. We used a procedure similar to one previously described (Lang et al, 2002). Namely, circles were superimposed on bright fluorescent spots in the FBXO32 (or LC3) channel and transferred to identical image locations in the endophilin channel. If the fluorescence intensity maximum in the endiophilin channel was located in the same quadrant of the circle and the morphology of the signal resembled that of the FBXO32 signal, the circle was rated as positive (colocalized). If not, the circle was rated as negative (not colocalized). Clusters for which a clear assignment was not possible were considered as neutral and excluded from further analysis. To be able to correct for random background colocalization, the circles were also transferred to a mirror image of the endophilin channel. Corrections were made to ensure that circles on the mirrored image were also placed within the cell. Both methods have yielded similar results.

Plasmids

The pCMV-SPORT6-FBXO32 plasmid was purchased from Thermo Scientific. The FBXO32-EGFP construct was generated by inserting mouse FBXO32 into pEGFP-N1 (Clonetech) using EcoRI and AgeI restriction sites. The pCherry-N1 plasmid was generated by replacing EGFP in pEGFP-N1 vector with mCherry (as published in Milosevic *et al*, 2011). The FBXO32-mCherry construct was generated by inserting mouse FBXO32 into pCherry-N1 using SalI and BamHI restriction sites. The pCAG-FBXO32-EGFP plasmid was generated by amplifying mouse FBXO32 and inserting it into pCAG-EGFP (Milosevic et al, 2011) using SalI and BamHI restriction sites. The pGEX-6P-1-FBXO32 plasmid was generated by inserting mouse FBXO32 using BamHI and EcoRI sites. A pCAG-EGFP-LC3 plasmid was generated by amplifying rat LC3 and inserting it into pCAG-EGFP (Milosevic et al, 2011) using BglII and SalI restriction sites. The endophilin A2-mRFP and endophilin A3-mRFP construct was generated by amplifying rat endophilin A2 and human endophilin A3 respectively and inserted them into pcDNA3.1-mRFP using BamHI and HindIII. All constructs have been verified by sequencing and restriction enzyme digestions. The constructs with the CAG promoter were verified in cultured fibroblasts before their use in neurons.

The pEGFP-LC3, pmRFP-LC3 and pGFP-Ub-G76V were purchased from Addgene. The pCAG-EGFP-N1 (Milosevic et al, 2011), pcDNA3.1-HA-Ubiquitin (rat; Cao *et al*, 2014), pEndophilinA1-mRFP (Perera et al, 2006), pmRFP-clathrin LC (Perera et al, 2006) were a gift from P. De Camilli (Yale University, New Haven, CT, USA)

Caspase activity assay

Caspase 3/7 apoptosis assay was performed with the ApoTox-Glo™ Triplex Assay (Promega) kit according to a modified version of the manufacturer’s protocol for 96 well plates. Cells were seeded (~10000 cells/well) in luminescence-compatible plates 24h before. Prior to the assay, cells were treated with 0.4M sorbitol for 1 hour to induce osmotic cell death, while others were left untreated to assess basal apoptotic levels. The cells were washed, and 40µl/well medium was added, including empty wells for blank reaction assessment. 10 µL/well Caspase 3/7 mixed reagent was added, incubated at RT in the dark on a rotational shaker. Untreated wells for each condition were reserved for protein quantification by the BCA protocol (Pierce). These cells were lysed with 75 µL/well of 1,5% n-dodecylmaltoside in PBS for 1 hour on an orbital shaker. Then, 59 µL dH_2O and 100 µL 1:25 BCA working solution were added, mixed and incubated for 30 min at 37°C. Samples were read on a Synergy H1 plate reader (Biotek) at 561 nm and normalized to a standard curve. Data were then normalized to the protein content for each condition.

Experimental work with Drosophila

Fly Stocks and genetics: Flies were grown on standard cornmeal and molasses medium at 25°C. The following Drosophila stocks were from the Bloomington Stock Center: w[*]; P{w[+mW.hs]=GawB}D42, y1 v1; P{TRiP.JF01340}attP2, y1 sc* v1; P{TRiP.HMS02671}attP4. P[w{+}UAS-Atg8-mCherry was obtained from T. Neufeld.

Immunohistochemistry and induction of autophagy: To induce autophagy, we either used starvation or stimulation. For starvation, early third instar larvae were placed on petri dishes containing 20% sucrose and 1% agarose for 4 h prior to experimentation 2. Immunohistochemistry of third instar larval NMJs was performed by dissecting larvae in HL3 on sylgard plates and then fixing with paraformaldehyde 4% in HL3 for 20 min. After 45 min permeabilization with 0.4% Triton X-100 in PBS larvae of different genotypes were physically marked and treated in the same tube for the labeling. Samples were preblocked with 10% NGS-PBT (0.1% Triton X-100 and 0.4% Triton X-100 in PBS, respectively) for 30-60 min and then incubated with primary antibodies overnight at 4°C. Samples were washed several times and then incubated with secondary antibodies in PBT with 10% NGS for 2 h at room temperature. The samples were finally mounted in Vectashield (Vector Laboratories).

Imaging and Antibodies: Fixed samples were imaged on a Nikon A1R confocal microscope through a 60X NA1.2 water immersion lens. Single confocal planes of boutons were scanned using identical settings. Fluorescence was quantified using NIH ImageJ: Average pixel intensities in boutonic areas were calculated or the number of mCherry-positive autophagosomes was measured using particle analysis of a binary image. The number of mCherry-positive autophagosomes was measured using particle analysis of a binary image by first applying a threshold mask and a selection of boutonic areas in a single plane of mCherry positive synapses.

Statistical analysis: Statistical significance was determined using GraphPad Prism software, Version 6 (Graphpad, San Diego, CA, USA. www.graphpad.com). Parametric data were analyzed with one-way analysis of variance tests (ANOVA), followed by Tukey-Kramer testing. Non-parametric data was analyzed using Kruskal-Wallis followed by Dunn's test. Significance of statistical difference was defined as ****$p<0.0001$, ***$p<0.001$, **$p<0.01$,*$p<0.05$, ns $p>0.05$.

Antibodies used for Western blotting

FOXO3a (Cell Signaling, rabbit, 75D8), 1:1000
P-FOXO3a (Cell Signaling, rabbit, Ser253), 1:1000
FOXO1 (Cell Signaling, rabbit), 1:1000
FBXO32 (Novus, goat), 1:1000
FBXO32 (ECM, rabbit, AX2045), 1:1000
ATG5 (Cell Signaling, rabbit) 1:1000
ATG9A (abcam, rabbit), 1:1000
ATG16L1 (MBL, rabbit), 1:1000
LC3B (Cell Signaling, rabbit, D11), 1:1000
ATG3 (Cell Signaling, rabbit, #3415), 1:1000
BECLIN1 (Cell Signaling, mouse) 1:500
HDAC6 (Millipore, rabbit, 07-732) 1:1000
UVRAG (Sigma Aldrich, rabbit, HPA016932) 1:1000
CDK5 (Santa Cruz, rabbit) 1:2000
GSK3B (Cell Signaling, rabbit) 1:8000
P-GSK3B (Cell Signaling, rabbit) 1:1000
HPRT (Abcam, rabbit) 1:1000
Ubiquitin (mouse FK2) 1:2000
Endophilin 1 (gift of P. De Camilli and SySy, both rabbit) 1:1000
Endophilin 2 (gift of P. De Camilli, rabbit) 1:1000

Antibodies used for immunolabelling

P-FOXO3a (Cell Signaling, rabbit, Ser253) 1:200
FBXO32 (Novus, goat), 1:200
LC3B (Cell Signaling, rabbit, D11) 1:1000
Synaptobrevin2 (SySy, mouse, 69.1) 1:500
GFAP (SySy, mouse, 64F6) 1:500
mCherry (Novus; chicken, NBP2-25158), 1:1000
DLG (DSHB; mouse, 4F3), 1:500
MAP2 (Chemicon, rabbit), 1:1000
Cleaved caspase-3 (Cell Signaling, rabbit), 1:600

Secondary antibodies used for immunolabelling

Anti-rabbit Alexa Fluor 488 (LifeTechnology, goat), 1:200 and 1:1000 (Drosophila)
Anti-rabbit Alexa Fluor 555 (LifeTechnology, goat), 1:1000
Anti-rabbit Alexa Fluor 594 (LifeTechnology, goat), 1:200
Anti-mouse Alexa Fluor 488 (LifeTechnology, goat), 1:200
Anti-mouse Alexa Fluor 594 (LifeTechnology, goat), 1:200
Anti-mouse Alexa Fluor 647 (Invitrogen) 1:400

Supplemental References

Bolte, S. and Cordelières, F.P. (2006). A guided tour into subcellular colocalization analysis in light microscopy, Journal of Microscopy 224, 3: 213-232.

Cao, M., Milosevic, I., Giovedi, S., and De Camilli, P. (2014). Upregulation of Parkin in endophilin mutant mice. J Neurosci 34, 16544-16549.

Capece, V., Garcia Vizcaino, J.C., Vidal, R., Rahman, R.U., Pena Centeno, T., Shomroni, O., Suberviola, I., Fischer, A., and Bonn, S. (2015). Oasis: online analysis of small RNA deep sequencing data. Bioinformatics 31, 2205-2207.

Chandrasekharan, K., Yoon, J.H., Xu, Y., deVries, S., Camboni, M., Janssen, P.M., Varki, A., and Martin, P.T. (2010). A human-specific deletion in mouse Cmah increases disease severity in the mdx model of Duchenne muscular dystrophy. Science translational medicine 2, 42ra54.

Dobin, A., Davis, C.A., Schlesinger, F., Drenkow, J., Zaleski, C., Jha, S., Batut, P., Chaisson, M., and Gingeras, T.R. (2013). STAR: ultrafast universal RNA-seq aligner. Bioinformatics 29, 15-21.

Lang, T., Margittai, M., Holzler H. and Jahn, R. (2002). SNAREs in native plasma membranes are active and readily form core complexes with endogenous and exogenous SNAREs. J. Cell Biol. 158:751-760

Liao, Y., Smyth, G.K., and Shi, W. (2014). featureCounts: an efficient general purpose program for assigning sequence reads to genomic features. Bioinformatics 30, 923-930.

Love, M.I., Huber, W., and Anders, S. (2014). Moderated estimation of fold change and dispersion for RNA-seq data with DESeq2. Genome Biol 15, 550.

Milosevic, I., Giovedi, S., Lou, X., Raimondi, A., Collesi, C., Shen, H., Paradise, S., O'Toole, E., Ferguson, S., Cremona, O., et al. (2011). Recruitment of endophilin to clathrin-coated pit necks is required for efficient vesicle uncoating after fission. Neuron 72, 587-601.

Perera, R.M., Zoncu, R., Lucast, L., De Camilli, P., and Toomre, D. (2006). Two synaptojanin 1 isoforms are recruited to clathrin-coated pits at different stages. Proceedings of the National Academy of Sciences of the United States of America 103, 19332-19337.

Rampon, C., Bouillot, S., Climescu-Haulica, A., Prandini, M.H., Cand, F., Vandenbrouck, Y., and Huber, P. (2008). Protocadherin 12 deficiency alters morphogenesis and transcriptional profile of the placenta. Physiological genomics 34, 193-204.

Wang, G.X., Zhao, X.Y., Meng, Z.X., Kern, M., Dietrich, A., Chen, Z., Cozacov, Z., Zhou, D., Okunade, A.L., Su, X., et al. (2014). The brown fat-enriched secreted factor Nrg4 preserves metabolic homeostasis through attenuation of hepatic lipogenesis. Nature medicine 20, 1436-1443.

Tian A., Baumgart T. (2009) Sorting of lipids and proteins in membrane curvature gradients. Biophys. J. 96, 2676–2688.

Yang, S., Farias, M., Kapfhamer, D., Tobias, J., Grant, G., Abel, T., and Bucan, M. (2007). Biochemical, molecular and behavioral phenotypes of Rab3A mutations in the mouse. Genes, brain, and behavior 6, 77-96.